Installation of perforated monopiles

And the associated fatigue damage

T. Twigt

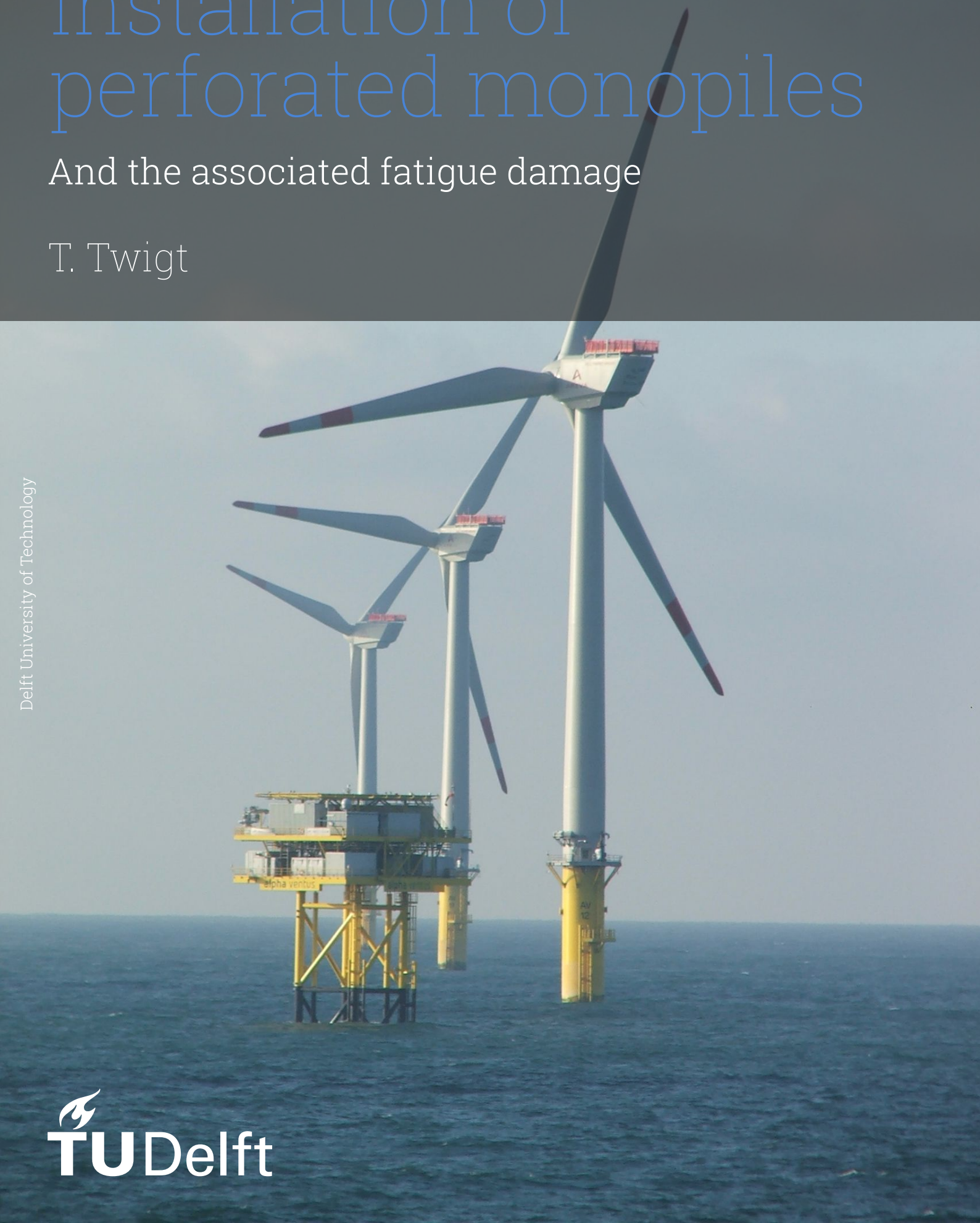

Delft University of Technology

TU Delft

Installation of perforated monopiles

And the associated fatigue damage

by

T. Twigt

A thesis submitted in fulfilment of the requirements for the degree of Master of Science at the Technical University Delft.

To be defended publicly on Friday, January 26th, 2024 at 15:00 in lecture room D of the faculty of Civil Engineering and Geosciences.

The work reported in this thesis was performed under the supervision of Marco Vergassola and Oriol Colomes Gene, whom I would like to thank for their guidance and support.

An electronic version of this thesis is available at `http://repository.tudelft.nl/`.

Project Duration: January, 2023 - January, 2024
Department: Offshore and Dredging Engineering, TU Delft

Cover: Wind turbines and electrical substation of Alpha Ventus Offshore Wind Farm in the North Sea [1]

TU Delft

Preface

Since 1972 we've known that climate breakdown is being caused by the use of fossil fuels.[2] At first the fossil fuel industry tried its best to deny and sow doubt about this reality[3], but with the help of climate scientists and activists, the issue of climate justice has received more attention. One could see climate change as a new challenge, unrelated to any of the fundamentals, but it's an extreme example of what happens when a system pretends the world has infinite resources and uses it as an infinite garbage bin.

Because of climate breakdown, a lot of effort, also at TU Delft, has been put into promoting the use of renewable energy and its development. It is one of the main reasons why I chose to study offshore engineering, and why most of my electives and indeed this thesis concern renewables. In contrast to what one may think, however, this growth in renewable energy hasn't been able to replace the use of fossil fuels. Instead, this growth in renewable energy has come in addition to growth in our emissions.[4] Furthermore, this growth in renewable energy has also come with a large environmental impact of its own, whether it is destroying forests and indigenous populations for the nickel mines in Sulawesi and West Papua [5], or slave labour for cobalt in Congo. [6]

This education into renewables, as valiant as its efforts may be, has done nothing to challenge the exploitative system we live in. Many educational and research projects at TU Delft begin with a problem that needs a technical solution. If there is, for example, not enough wind energy to go around, we can try, as in this thesis, to come up with a technical solution to get offshore wind turbines in deeper waters in a cost-effective manner. Research into this topic teaches me about structural dynamics, fatigue damage, design codes, pile driving, and much more which is part of the training to become an engineer.

But what this type of research also teaches me, is that for every possible problem, I should look for a 'techno-fix'. No matter how tough the problem is, we smart people at TU Delft will engineer ourselves out of it. Offshore oil rigs pollute too much? Just put a wind turbine on top of it, so we can use green energy to drill for oil.[7] Of course this reduces pollution, but is it the only solution?

The 'hidden curriculum', as a friend recently described it [8], is so all-encompassing and self-evident, that we don't even realize that this is what students are being taught. During my studies at TU Delft, I have tried - far too little and far too late I might add - to challenge this narrative. I've helped organize a protest and occupation at TU Delft, which demanded that the TU Delft become a place of education and research free from interference from the fossil fuel industry. I've also helped in organizing teach-ins about the ongoing atrocities in Israel and Palestine, asking the question if we at TU Delft should still help develop weapons in partnership with a government that is being charged with genocide.

Some students and staff members agree with these demands, and others do not, but I'm glad that at least in some small way I've been able to help start these debates. The reply from the TU Delft board, however, has been less than welcoming. Police dragged students from End Fossil out of the university [9], and in response to a teach-in about Israel/Palestine, security first tried to censor our language, with the board later accusing us of polarizing, saying that "freedom of speech has no place on campus". [10]

This preface isn't meant as an attack on 'techno-fixes'. I still believe that technology, as discussed in this thesis, can help improve the quality of our lives. I wish that beyond these technological improvements, students and staff would also be more involved in the political aspects of education and research. For whom are we developing technologies, and to what ends? What are we learning students, and in whose interests? The answers to these questions are deeply political and ideological, and deserve a discussion if we want education to be, as Paulo Freire said, "an instrument of liberation".[11]

T. Twigt
Delft, January 2024

”If the completion of the technological project involves a break with the prevailing technological rationality, the break in turn depends on the continued existence of the technical base itself. For it is this base which has rendered possible the satisfaction of needs and the reduction of toil — it remains the very base of all forms of human freedom. The qualitative change rather lies in the reconstruction of this base — that is, in its development with a view of different ends.”

Herbert Marcuse, in ”One-Dimensional Man” [12]

Summary

The European offshore wind industry has experienced significant growth in the past decade, mainly focusing on shallow areas in the North Sea to reduce the Levelised Cost of Electricity (LCoE) and compete with fossil fuels. However, as shallow areas become scarcer and the industry seeks greater independence from government subsidies, a shift towards deeper waters is anticipated, and already observed in Europe. In the northern part of the North Sea (60-120 meters deep), jacket foundations are currently favoured, despite drawbacks such as extensive engineering efforts, weld requirements, challenging series production, and high costs. This misalignment with the industry's LCoE reduction goal highlights the need for a technologically viable and economically attractive foundation concept for waters in the 60-120-meter range.

To combat this challenge, perforated monopiles are being developed. The perforated monopile consists of a monopile with perforations, either circular or elliptical, around the splash zone, with the goal of reducing the frontal area, and thus reducing the hydrodynamic loads on the structure. These concepts aim to combine the ease of manufacturing of a monopile, with the reduced area affected by hydrodynamic loads that are common for jacket structures. The research done so far on these perforated monopiles has only looked at the reduction in hydrodynamic loads, which have proven significant. These reductions in hydrodynamic loads should enable the perforated monopiles to be used in deeper waters compared to regular, non-perforated, monopiles. They could provide a tempting alternative for the more expensive jacket structures, but more research is necessary, especially in analyzing other loads that the perforated monopile may be subject to.

This thesis aims to look at one such different load that affects this perforated monopile, namely the installation loads induced by hammering. The first part of this thesis will look at stresses and fatigue damage during the installation of non-perforated monopiles. The second part will analyze the increased stresses, possible losses in hammer energy, and increased fatigue damage, all due to the presence of perforations. Finally, several alternatives, such as different geometries of perforations and different hammer loads will be analyzed with regard to their effect on fatigue damage.

The fatigue damage due to installation is found to increase significantly due to the presence of perforations, increasing from 5% for non-perforated monopiles, to up to 118% and 112% for the two most promising geometries analyzed, thus proving a show-stopper for installation via impact hammer, if no measures are taken.

Changing certain parameters, however, either the geometries of the perforations, or the characteristics of the hammer used, shows that installation is indeed possible. Using different geometries of perforations, that maintain a significant reduction in area, shows installation is possible, whilst limiting the fatigue damage to 53%. A reduction in hammer force by a factor of 2, also decreases the fatigue damage by 34% on average. The use of a so-called vibro-hammer also shows promising, resulting in a halving of the fatigue damage compared to the use of an impact hammer, but more research needs to be done to confirm this final finding.

To conclude, this research shows that installation of a perforated monopile is possible, although most, if not all of the reduction in fatigue damage due to hydrodynamic loading is cancelled out by the increase in fatigue damage due to installation. Geometries and installation methods may exist that improve the fatigue life of the structure, but this research was unable to find them. Future research may be able to find geometries and installation loads that do reduce overall fatigue damage.

Further research is also necessary before perforated monopiles can be taken into service, such as the confirmation of the energy losses in installation due to perforations. Also, several other load cases need to be analyzed, to ensure the perforated monopile survives its designed lifetime.

Contents

Preface i

Summary iii

1 Introduction 2
- 1.1 Trends in offshore wind . . . 2
- 1.2 Type of support structures . . . 4
  - 1.2.1 Monopiles . . . 6
  - 1.2.2 Jackets . . . 6
  - 1.2.3 Gravity based . . . 7
  - 1.2.4 Floating . . . 7
- 1.3 Perforated monopiles . . . 7
- 1.4 How are (perforated) monopiles installed? . . . 9
- 1.5 Research gap . . . 12
- 1.6 Research questions . . . 12

2 Methodology 13
- 2.1 Thesis approach . . . 13
  - 2.1.1 Phase 1: Fatigue damage during installation of non-perforated monopiles . . . 13
  - 2.1.2 Phase 2: Fatigue damage during installation of perforated monopiles . . . 13
  - 2.1.3 Phase 3: Optimizing . . . 15
- 2.2 Software used . . . 15
  - 2.2.1 GRLWEAP 14 . . . 15
  - 2.2.2 Ansys Workbench 2022 R2 . . . 16
  - 2.2.3 Microsoft Excel 2019 . . . 17
  - 2.2.4 MATLAB R2023b . . . 17
  - 2.2.5 Overleaf . . . 17

3 Installation of a non-perforated monopile 18
- 3.1 Reference monopile . . . 18
- 3.2 Hammer force . . . 18
  - 3.2.1 Perikleous et al. . . . 19
  - 3.2.2 Deeks and Randolph . . . 19
  - 3.2.3 GRLWEAP . . . 20
- 3.3 Resistance to Driving . . . 21
- 3.4 Fatigue damage . . . 23
- 3.5 Summary and results . . . 25

4 Installation of a perforated monopile 27
- 4.1 Ansys model . . . 27
- 4.2 Stress concentrations . . . 28
- 4.3 Force throughput . . . 29
- 4.4 Fatigue damage . . . 31
- 4.5 Summary and results . . . 32

5 Conclusion and possible alternatives 33
- 5.1 Model comparison . . . 33
  - 5.1.1 Stress comparison . . . 33
  - 5.1.2 Blow count . . . 34
  - 5.1.3 Fatigue damage . . . 35
- 5.2 Research questions . . . 35
  - 5.2.1 Non-perforated monopiles . . . 35
  - 5.2.2 Perforated monopiles . . . 36

5.2.3 Energy losses . . . 36
5.2.4 Fatigue damage . . . 36
5.3 Possible alternatives . . . 36
5.3.1 Geometries . . . 36
5.3.2 Vibratory hammer . . . 37
5.3.3 Reduction in hammer force . . . 38

6 Discussion and recommendations 40
6.1 Discussion . . . 40
6.2 General recommendations . . . 40
6.2.1 Loss of energy due to perforations . . . 41
6.2.2 Simplified model . . . 41
6.3 Future research . . . 41
6.3.1 Other geometries . . . 41
6.3.2 Other loads and failure modes . . . 42
6.3.3 Other hammers . . . 42

References 43

A Additional figures and code 47

B Additional figures for reduced force input 51

List of Figures

1.1 Exponential growth of worldwide installed capacity of offshore wind throughout the years [13] . . . 2
1.2 Water depth of offshore wind turbines throughout the years [19] . . . 3
1.3 Water depth in the North Sea with the locations of various wind farms[20] . . . 4
1.4 Foundation concepts and their share on commercial projects as of late 2012. (a) Gravity-based foundation (16%), (b) monopile foundation (74%), (c) caisson foundation (0%), (d) multiple foundation (5%), (e) multi caisson foundation (0%) and (f) jacket foundation (5%).[22] Since 2012, floating substructures have also become part of the foundation mix. 4
1.5 Offshore wind substructure technology used in announced projects [19] . . . 5
1.6 Monopile foundation for an offshore wind turbine. . . . 6
1.7 Perforated monopile design [34] . . . 8
1.8 The three perforation geometries that are analysed in previous research [35] . . . 8
1.9 The first drivability analysis [37] . . . 9

2.1 The introduction of the perforations in monopile in Ansys in 6 steps, according to the dimensions from geometry 2, explained in chapter 4, and fixed to the bottom . . . 14
2.2 Close up of the smallest mesh used for geometry 1, using elements of size 0.2 meters . 16

3.1 Monopile dimensions [35] . . . 19
3.2 Force signal of IHC-S4000 as measured in previous research [53] . . . 20
3.3 Force signal of IHC-S4000 as determined based on previous analytical work [54] See the source code in Appendix A . . . 20
3.4 Force signal of IHC-S4000 generated by GRLWEAP per millisecond . . . 21
3.5 SRD for the non-perforated monopile from this thesis . . . 22
3.6 Stresses along the height of the monopile due to hammering. The GRLWEAP graph is shown in the middle, the graph on the right is from Ansys results . . . 24
3.7 Stress concentrations along the height of the monopile at the relevant time steps . . . 25

4.1 The three perforation geometries that are analysed in previous research [35] . . . 27
4.2 The full dimensions of the simplified model for geometry 2. Other geometries use the same centre points for each perforation, with different width and height . . . 28
4.3 The stresses for geometry 2 as computed by Ansys for a mesh size of 0.5 meters at 7 milli-seconds . . . 28
4.4 A close-up of the stresses for geometry as computed by Ansys for a mesh size of 0.5 meters at 7 milli-seconds. . . . 29
4.5 The stress concentrations for various geometries over time . . . 29
4.6 Velocity of the probe just below the perforations for all geometries in m/s . . . 30
4.7 Reaction force at the bottom of the model for all geometries . . . 31

5.1 Geometry 4 (b) and 5 (a) . . . 37
5.2 Hammer force over time, using an efficiency of 41.5%, as opposed to the efficiency of 83% used elsewhere in this thesis. . . . 39

A.1 Force wave propagation through perforated monopile with geometry 1 using an element size of 0.2 meters. The stresses are displaced at 5, 7, 11 and 20 milli-seconds . . . 48
A.2 All the soil parameters used as an input for the GRLWEAP software, which is used as a resistance for the wave equation . . . 49
A.3 Mesh convergence for the stresses in the perforated monopile with geometry 2 with the element size in meters . . . 49

A.4 Mesh convergence for the reaction force in the perforated monopile with geometry 2 with the element size in meters 50

B.1 The maximum stress concentration observed in all geometries of the perforated monopiles over time, using half the installation force available in IHC-S-4000 51
B.2 The reaction force at the bottom of the model for all geometries over time, using half the installation force available in IHC-S-4000 52
B.3 The velocity of the probe located 30m from the bottom of the model in all geometries of the perforated monopiles over time, using half the installation force available in IHC-S-4000 52

List of Tables

1.1 Geometry dimension, where a is perforation width and b is perforation height. β is the reduced area 8

3.1 Material properties of the tower 18
3.2 Soil properties at installation location [51] 22

4.1 Geometry dimension, where β is the reduced area 27
4.2 Reduced area β, maximum reaction force, velocity, stress concentrations, required blows and fatigue damage for the different geometries analyzed. 32

5.1 Parameters and results for the different geometries analyzed. 34
5.2 Reduced area β, stress concentrations, required blows and fatigue damage for the different geometries analyzed. 37
5.3 Parameters and results for the different geometries analyzed for the vibrohammer QUCV640 with penetration up to 28m. 38
5.4 Stress concentrations, required blows and fatigue damage for the different geometries analyzed with half the force. 39

1

Introduction

This chapter aims to provide the reader with an overview of the historical trends in offshore wind, and of what the future may hold, especially concerning the development of new types of monopile foundations for offshore wind turbines.

1.1. Trends in offshore wind

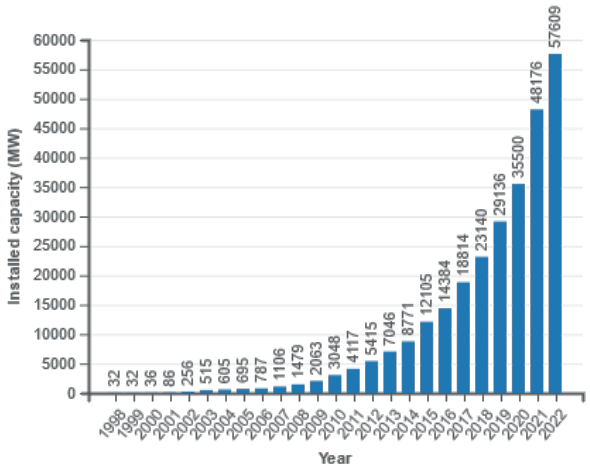

Figure 1.1: Exponential growth of worldwide installed capacity of offshore wind throughout the years [13]

The first offshore wind farm was built in 1991 in Denmark, and paved the way for the offshore wind industry. 11 wind turbines with a capacity of 450 kW per turbine were built at a water depth of 4 metres, and at a distance of 2 km to the shore. [14] In the 30 years following this historical step, incredible progress has been made, and the average size of wind turbines installed in 2020 was already 8.2 MW. [15] As can be seen in figure 1.1 above, the installed capacity of offshore wind around the world has been growing exponentially ever since its inception in 1991.

Despite this exponential increase in offshore wind capacity, however, it would be unfair to state that the energy transition has begun. A transition is when you do more of one thing (renewables) and less of the other (fossil fuels). There has been an increase in renewables, but so far this has been accompanied by an increase in the use of fossil fuels as well. So far we've only reached a renewable energy 'addition', not a transition.[4] If we are to start the energy transition, and if we want to maintain our energy-rich lifestyle, an even further increase in renewable energy, and consequently offshore wind capacity, is required.

Facing this reality, the European Union and the Dutch government have announced ambitious plans to increase their offshore wind capacity further. The Dutch government is planning an installed capacity

of 11.5 GW by 2030, up from just 1 GW in 2020. [16]. The European Union has planned a capacity of 60 GW by 2030, and a stunning 300 GW by 2050, up from a capacity of just 14.6 GW in 2021.[17] A large part of this offshore wind capacity is to be built in the North Sea.

The offshore wind industry is gradually being compelled to venture into deeper waters due to the projected growth and decreasing availability of shallow areas. Despite the challenges that come with this, wind farm developers are attracted to far offshore locations because of the higher average wind speeds and power densities. [18] Consequently, a turbine installed in a far offshore location with high wind potential can generate more power over time than one placed in less favourable wind conditions. This leads to a reduction in the Levelized Cost of Energy (LCoE) since more power is produced for the same capital cost requirements, bolstering the business case for developing far offshore wind farms. This increase in water depth has also been accompanied by an increase in the average distance to the shore of offshore wind farms. [19]

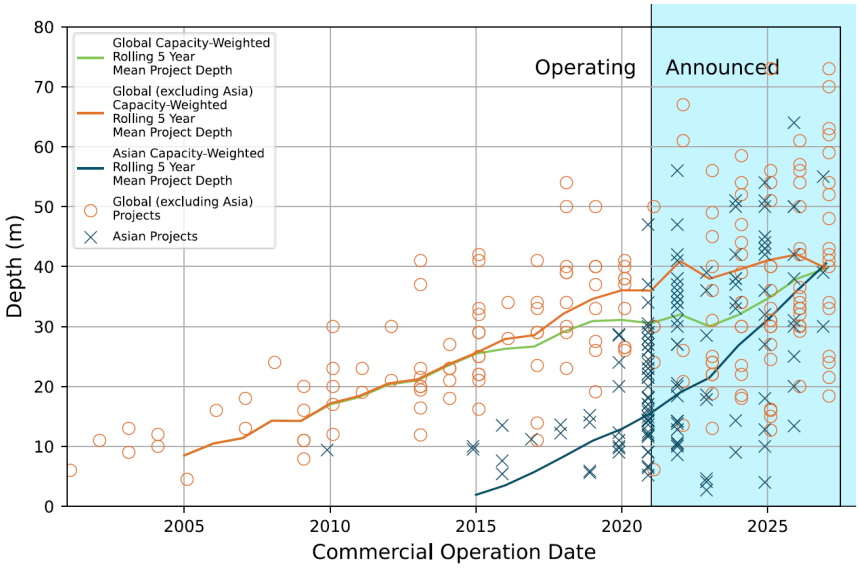

Figure 1.2: Water depth of offshore wind turbines throughout the years [19]

This trend of increasing water depth is visible in the history of turbines installed over the years, and the projection of turbines announced to be installed. [19]. The first turbines were installed at a depth of just a couple of meters. In 2022 a water depth of 30 meters has become the norm, as can be seen in figure 1.2 Since shallower waters are becoming less and less available, a transition to deeper waters is expected, given the immense expected growth.

A large part of this expected growth of The Netherlands and the EU is expected to take place in the North Sea. As can be seen in figure 1.3, a large part of the North Sea is between 60 and 120 metres deep. This is an area which is close to industrialised countries that use a lot of energy. Furthermore, this is a very windy area, making it an excellent choice for offshore wind farms. [18] As will be explained in the following chapters, this thesis aims to explore the feasibility of installing a new foundation concept in this area with a water depth of 60-120 metres.

Another part of what is making this projected growth in offshore wind possible is the sharp reduction in costs accomplished by the industry. Where the wind farms of the past relied heavily on government subsidies to turn a profit, In 2018 however, the first subsidy-free tenders for offshore wind farms in The Netherlands were won. The costs for wind farm Borssele have been reduced to €54.50 per MWh, and offshore wind has begun to compete with traditional fossil fuels in terms of cost. This has increased the incentive for governments to promote offshore wind as an important part of their plans for the energy transition.[21]

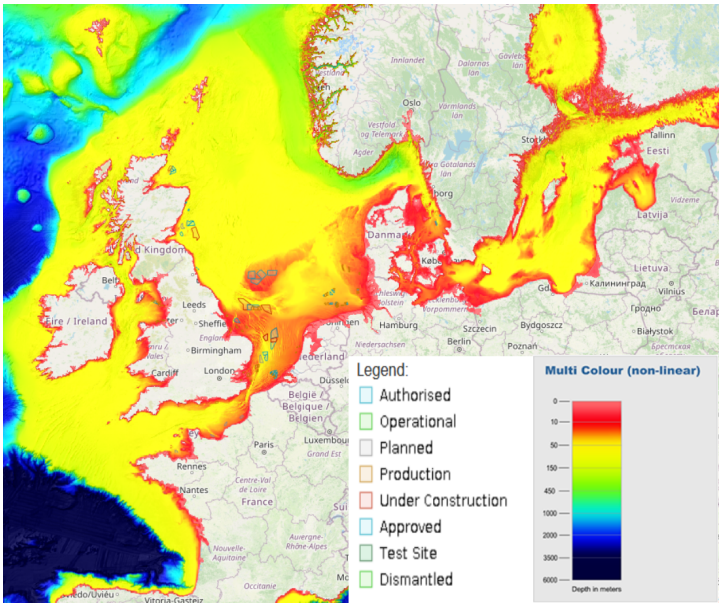

Figure 1.3: Water depth in the North Sea with the locations of various wind farms[20]

1.2. Type of support structures

Offshore wind turbines can be divided up into two parts: the rotor-nacelle assembly (RNA) and the support structure. The blades make up the rotor, while the electro-mechanical components are housed in the nacelle. The support structure, on the other hand, encompasses all the elements that provide support for the RNA. In most instances, the support structures are divided into a tower, a sub-structure, and a foundation.

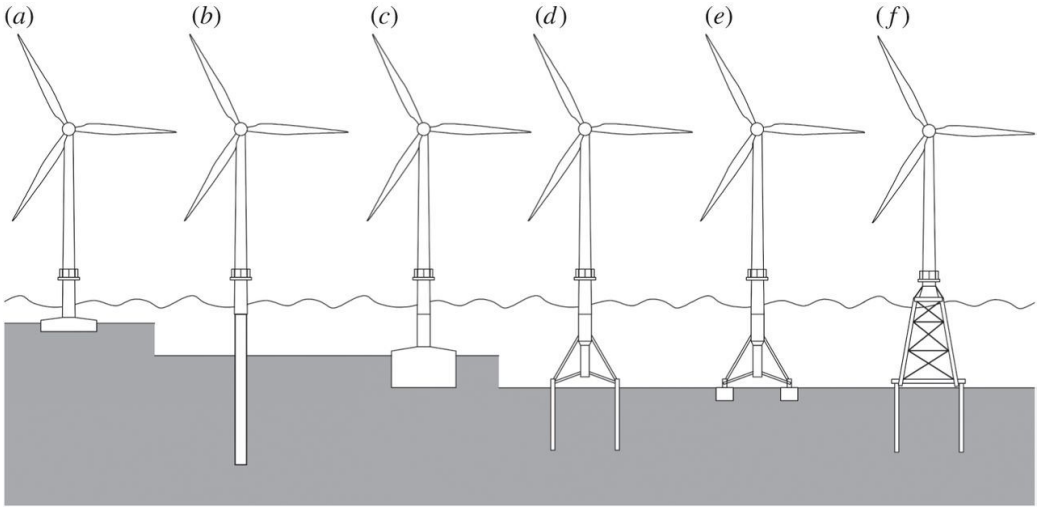

Figure 1.4: Foundation concepts and their share on commercial projects as of late 2012. (a) Gravity-based foundation (16%), (b) monopile foundation (74%), (c) caisson foundation (0%), (d) multiple foundation (5%), (e) multi caisson foundation (0%) and (f) jacket foundation (5%).[22] Since 2012, floating substructures have also become part of the foundation mix.

The tower, which is typically tubular and conical in shape, is a component that is found in onshore wind turbines as well. The sub-structure is the part of the turbine between the interface level and the seabed. The components below the seabed are referred to as the foundation. The wind turbines that are currently used by the industry, along with their market shares, are shown in figure 1.4.

As of the end of 2021, monopiles continue to be the primary type of foundation, constituting 74.7% of the overall offshore wind foundation market for reported installed projects. Jacket substructures are the second most prevalent type of foundation, accounting for 13.2% of reported operating substructures.

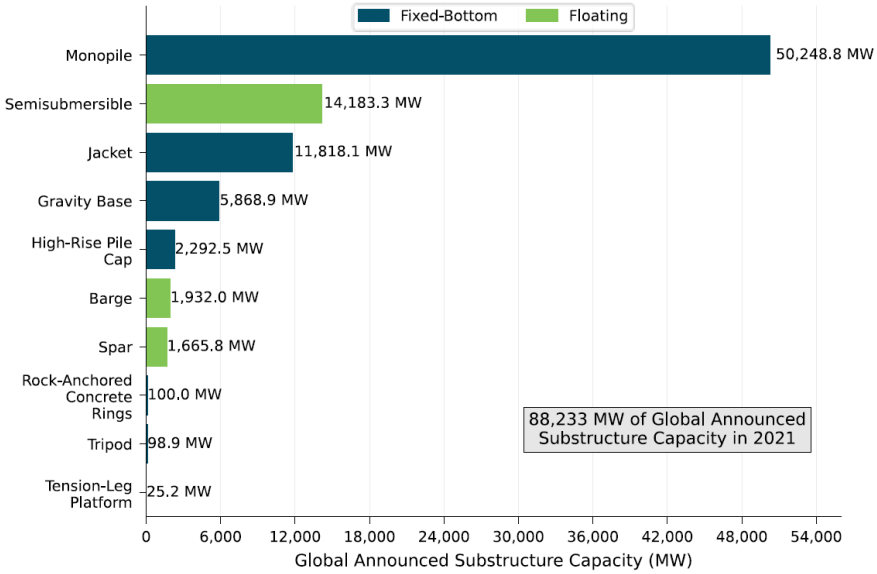

Figure 1.5: Offshore wind substructure technology used in announced projects [19]

The mix of support structures that have been announced for future projects can be seen in figure 1.5. For future foundation types, the share of monopiles drops slightly to 57.0%, but because monopile production is a well-established process that has been industrialized, monopiles typically have a cost advantage and are projected to maintain their dominance. [23]

A simple way in which the force on the structure caused by the hydrodynamic loads can be obtained is via the Morison equation:

$$F = \frac{\pi}{4}\rho_w C_M D^2 \cdot \dot{v} + \frac{1}{2}\rho_w C_D A v^2 \tag{1.1}$$

where F is the total hydrodynamic force, C_M is a dimensionless inertia coefficient, D is the pile diameter, $\dot{v}$ is the water acceleration, ρ_w is the seawater density, C_D is the coefficient of drag, A is the affected area, and v is the water velocity. As can be noted from the Morison equation, the drag load is dependent on the area and diameter of the monopile. Reducing this area could hence reduce the hydrodynamic loads.

The Morison equation consists of two terms: the first represents the inertial force, while the second represents the drag force component. These terms are dependent on water velocity and acceleration.

The Morison equation is a useful first estimate but makes several assumptions:

- Steady and uniform flow, as opposed to waves.
- Simplicity of the structure. The equation does not account for specific flow interactions and turbulence patterns associated with, for example, perforated geometries.
- No nonlinear effects
- No fluid-structure interactions arise when the structure is deformed due to the waves. These interactions do occur and may affect the loads

Despite these assumptions, a reasonable estimate of hydrodynamic forces can still be made. However, a higher-order wave theory may be required for a more detailed evaluation of hydrodynamic forces in the future.[24] All bottom fixed foundations are subject to this hydrodynamic load, which is assumed to reduce with a reduced area.

All types of structures are subject to aerodynamic loads from the rotor, which are dominated by lift force, and are highest at the rated wind speed, usually around 10 m/s. Furthermore, all foundations are also subject to gravitational loads from the RNA. In the following sections, a brief description of the different foundation types is given.

1.2.1. Monopiles

Monopiles are single circular steel piles that are usually driven into the seabed in shallow to intermediate water depths of up to 40m. [25]. The extensive adoption of monopiles has resulted in a substantial level of industry maturity and standardization. Consequently, organizations such as Det Norske Veritas Germanischer Lloyd (DNVGL) have released comprehensive design protocols that are highly regarded and implemented by the industry. [26]

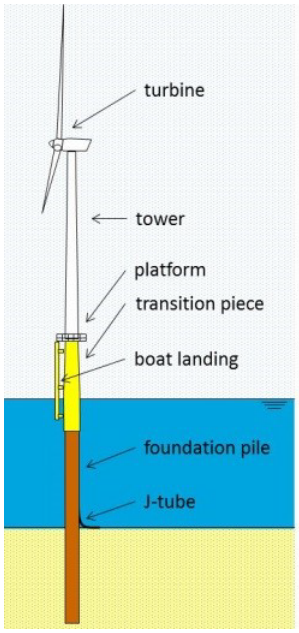

Figure 1.6: Monopile foundation for an offshore wind turbine.

The working principle behind the monopile concept is that horizontal hydrodynamic and aerodynamic loads are transferred laterally into the soil. Figure 1.6 presents a monopile, and its main components:

- Turbine: The RNA that turns wind energy into electrical energy
- Tower: Conical element on top of the transition piece, that supports the RNA
- Transition piece: The transition piece provides a base on top of, and often overlapping the monopile for the positioning of the tower.
- Foundation pile: Tubular part to transition the loads into the soil. Sometimes a conical diameter reduction takes place at the top of the pile.

In deeper waters fatigue loads and mechanical stresses due to waves become too large for the turbine to survive its intended lifetime. This is especially true for larger turbines, as the moment will become bigger, and as the increased diameter of the monopile causes larger hydrodynamic loads.

1.2.2. Jackets

Jackets are essentially large steel frames consisting of three or four legs. The legs are typically tubular and connected by a series of braces and horizontal members, forming a lattice-like structure. While jacket foundations are economical in terms of steel consumption, they can be costly when it comes to design, construction and installation.[27] Given this economic trade-off jacket structures are expensive when placed in shallow waters, but become economically attractive when the water depth exceeds the 40 meter range. [28] These tubular structures have their origin in the oil and gas industry.

For installation, the foundation piles are set into an installation frame. This is a template structure that allows for tight tolerances. After this, the hammering procedure starts. In this phase the piles are driven into the seabed, similar to the case of a monopile. The jacket structure is lowered on top of these foundation piles with the help of locating cones. After this, the connection between the piles is often filled with concrete and secured in place. In some other cases, suction caissons are used to keep the foundation in place.[29]

1.2.3. Gravity based

Gravity-based foundations are made up of a concrete slab based on a firm soil or rocky seabed to avoid tensile loads between the foundation's bottom and the soil surface. This is accomplished by ensuring adequate dead loads. The size of the base can be adjusted based on the soil conditions to ensure adequate bearing capacity. The concrete base slab can be fitted with small skirts and will require some form of scour protection in all locations. In the offshore industry, these foundations are advantageous when the environmental loads are not too high. Ballast can be added to increase the dead loads, and temporary structures like mud mats are also considered part of this type of foundation. [26] Up until 2018 in Europe, gravity-based foundations for offshore wind farms were uncommon and have only gone down to a depth of 20 metres.[30]. The market share is expected to increase in the following years. [19]

1.2.4. Floating

Wind turbines float in water by the buoyancy and stability generated by a concrete, steel, or hybrid structure on top of which the turbines are installed. These floating foundations are stabilised by moorings and anchors, and by the distribution of weight within the structure. As can be seen in figure 1.5, most of the announced floating support structures are so-called 'semi-submersibles'. This design consists of usually three of four vertical cylinders, that are joined together by braces to create a surface upon which the turbine can be installed.

Floating offshore wind turbines are a relatively new technology. The first prototype of a floating wind turbine was built in 2009 by the Norwegian company Statoil (now Equinor) and was installed in the North Sea. The prototype, known as the Hywind, was a 2.3 MW turbine mounted on a floating spar buoy anchored to the seabed. [31]. In the following years, other prototypes were developed, on a similar scale as the Hywind prototype. Since 2017 the technology has continued to advance, with larger turbines being developed and more projects being launched around the world. As of 2021, there are over 60 floating offshore wind projects in various stages of development or operation, with a total capacity of over 3 GW. [32]

For now, floating wind is a promising but expensive technology. The LCOE for floating wind farms built in 2020 is estimated at €200/MWh, about 3 times as high as bottom-fixed turbines. In the coming years, these costs are expected to decrease making it competitive with bottom-fixed foundations. [19]

However, designing mooring systems for shallower waters (50 - 100m) can be extremely challenging. During the transition from linear to nonlinear response in tension, there is a potential for extremely large tension in the mooring line during harsh environmental conditions, when the semi-submersible has large movements. This extreme mooring tension can be mitigated by designing a soft mooring line, but this brings with it its own challenges, like chain link diameter and weight limitations. [33]

1.3. Perforated monopiles

Recently, investments have been made into researching perforated monopiles. [34] This concept introduces perforations around the waterline in regular monopiles, as can be seen in figure 1.7. As we've seen from the Morison equation described above, a reduction in frontal surface area should bring with it a reduction in hydrodynamic forces. In other research, three different geometries of perforations are analyzed, which are shown in figure 1.8 [35]

The research furthermore shows that the relationship between reduction in force on the monopile and reduction in area size subject to hydrodynamic loading is far from linear. Rather, the research done so

Figure 1.7: Perforated monopile design [34]

far concludes that this relationship is instead dependent on the so-called 'KC number' of specific sea states. [35] [34] The reduction in hydrodynamic forces and fatigue loading for all analysed geometries can be seen in table 1.1, and is compared to a reference monopile without perforations with a 10 metre diameter in 120 metre water depth. For more details, see the research done before which focussed on the reduction in hydrodynamic loads. [35] [34]

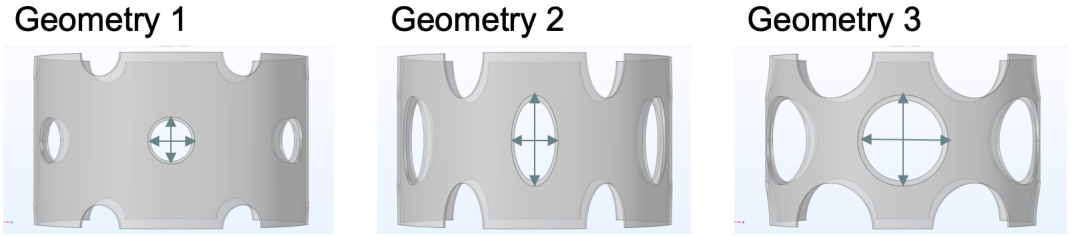

Figure 1.8: The three perforation geometries that are analysed in previous research [35]

-	Geometry 1	Geometry 2	Geometry 3
width [m]	1.6	1.6	3.1
height [m]	1.6	3.1	3.1
β [%]	12.9	24.8	48.6
Force reduction [%]	0	7	25
Fatigue reduction [%]	2.8	35.5	66.8

Table 1.1: Geometry dimension, where a is perforation width and b is perforation height. β is the reduced area

The most recent analytical research concludes that the use of a perforated model allows for the deployment of a 15MW turbine up to a water depth of 87 meters, whereas a monopile without perforations was not able to pass the fatigue check for any of the tested water depths (starting at 60 meters). [35] Moreover, by implementing this solution at shallower depths for monopiles, there is the potential for a substantial decrease in the overall steel quantity needed. Consequently, this would ultimately lead to a reduction in the cost of manufacturing monopiles.

This perforated type of foundation seems ideal for large parts of the North Sea. As previously discussed, the more shallow areas of the North Sea are becoming more scarce. Regular monopiles are unfit for deeper waters, and jackets and other structures bring with them large costs. Floating structures are still expensive, and it's unsure if these will be viable for the water depth range between 60 and 120 meters. [33] The perforated monopile combines the low area subject to wave loading that we know from jacket structures, together with the simplicity of a monopile.

1.4. How are (perforated) monopiles installed?

Since the perforated monopile is a relatively new concept, little is known of how it should be installed. As such this thesis will first take a look at how a regular monopile is installed, and consequently take a look at options for the installation of a perforated monopile.

Installation vessels for offshore monopiles are either jack-ups that stand firmly on the seabed during installation or motion-compensated crane vessels. From this position, a crane lifts a monopile into place. The monopile is kept in place by pile-handling tools like gripper devices, while the monopile is driven into the sea floor. [29] There is interesting research being done into the gentle driving of piles, but for now nearly all of the monopiles are driven into the seabed hydraulically to reach the desired penetration depth. [36]

The installation of offshore wind turbines is done in various steps that differ per wind farm, but most commonly occurs in three phases:

- Driving of foundation
- Installation of the transition piece
- Installation of tower (and nacelle/blades)

In the interest of both time and financial considerations, the amount of phases should be as low as possible, as should be the time per phase.

Before the monopiles can be driven into the seabed, a drivability study is done to determine the required number of blows and the hammer type required to reach the desired penetration depth.

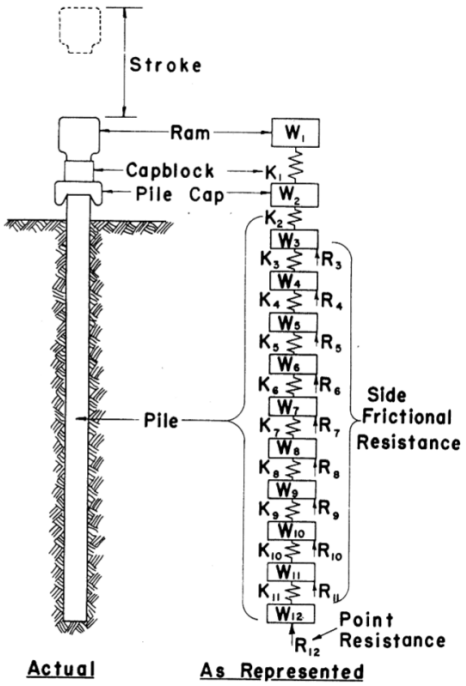

Figure 1.9: The first drivability analysis [37]

The first pile drivability and stress analyses were performed in 1960. [37] This research modelled the piles as a mass-spring system, as can be seen in figure 1.9. The pile was divided up into many masses, connected to each other with a spring. The top mass is impacted by the hammer, sending a wave through the pile, which causes the pile to slide into the ground. The side is modelled as a frictional resistance.

Ever since this research, several additional models have been made to improve on this original mode. [38] [39] These models were accurate as long as the diameter was small compared to the excited wavelengths in the structure, which are caused by hammer impact. Given the increase in size, the effects of stress wave dispersions have to be included. Newer research includes the effects of lateral inertia in larger diameter monopiles. The impact of lateral inertia is accounted for by incorporating the Rayleigh-Love correction term into the governing equations. Meanwhile, the soil is represented using distributed nonlinear springs and dashpots, following the traditional approach. [40]

Modelled as a linear homogeneous elastic rod, the governing equation is

$$\rho A\frac{\partial^2 u}{\partial t^2} - EA\frac{\partial^2 u}{\partial z^2} + R_s - [\rho v^2 I_p \frac{\partial^4 u}{\partial t^2 \partial z^2}] = 0 \tag{1.2}$$

in which ρ is the density of steel, A is the area of the pile, u is the displacement, t is time, E is the Young's modulus, R_s is the non-linear frictional resistance of the soil and I_p is the polar second moment area of the cross-section. The term in square brackets is the additional Rayleigh-Love correction term, which is not included in the original wave equation model. [37] The axial stress in the pile can be computed as

$$\sigma(z,t) = E\frac{\partial u}{\partial z} + [v^2 r^2 \frac{\partial^3 u}{\partial t^2 \partial z}] \tag{1.3}$$

where σ is the stress and$r_g = \sqrt{I_p/A}$ is the radius of gyration. The term in between square brackets is the added Rayleig-Love correction term. [40]

To determine drivability, first, the Soil Resistance to Driving (SRD) is determined. This SRD is used to determine the amount of hammer blows required and to determine the maximum compressive and tensile stresses in the pile. These stresses and blow counts are combined to estimate the fatigue damage. [41][42]

The SRD is typically derived by adjusting the calculation used to determine the ultimate static axial pile capacity in compression. A recent paper [43] refers to two design codes available [44] [45] In this paper, a designer is provided with guidance to determine shaft friction f and end bearing q in order to calculate the ultimate bearing capacity Q_d:

$$Q_d = Q_f + Q_p = fA_s + qA_p \tag{1.4}$$

with:
- Q_f = skin friction resistance,
- Q_p = total end bearing,
- f = unit skin friction capacity
- A_s = side surface area of pile
- q = unit end bearing capacity
- A_p = gross end area of pile

New research [41], along with standard design codes [44] [45] [26] [46] provide excellent design guidelines for determining fatigue damage, including calculations for the Stress Concentration Factor (SCF). The new research [41] states that cumulative fatigue damage D is evaluated with the Palmgren-Miner rule:

$$D = \sum_{n=i}^{\infty} \frac{n_i}{N_i} \tag{1.5}$$

with N_i = number of cycles before failure occurs for a given stress ratio variation $\Delta\sigma_i$, and n_i = number of cycles inflicted to the structure for the $\Delta\sigma_i$ stress variation. The design code provides guidance on the fatigue design of offshore steel structures and more precisely on the calculation of the stress concentration factors to be adopted in fatigue analysis. [26] The design guide [26] also provides S-N fatigue curves and is the industry-accepted standard for determining fatigue damage in offshore structures. It deviates from the other mentioned codes in that it is also used for monopiles, and not just jackets with smaller diameter piles.

The correlation between the soil resistance to driving (SRD) and blow count can be determined by utilizing readily accessible pile driving software packages like GRLWEAP, TNOWAVE, and others. These software packages employ the wave equation method to analyze the interaction between the hammer, pile, and soil in a given combination.

Based on the original model [37] described above the available software packages like GRLWEAP can simulate the motions and forces experienced by the foundation pile during the driving process using an impact hammer. These software packages then calculate the following outputs:

- The blow count required to reach a desired penetration depth
- The axial stresses in the monopile, distributed over the cross-section
- The energy transmitted by the hammer to the pile
- The pile velocity and displacements along the pile for certain pile penetration and associated capacity values.
- The residual stresses remaining in the pile between hammer blows.

Based on these results the following can be indirectly determined:

- The pile's bearing capacity at the time of driving or restriking, given its observed penetration resistance (blow count).
- The stresses during pile driving, given an observed blow count.
- The expected blow count if the static bearing capacity of the pile is known (e.g., from a static soil analysis)

GRLWEAP solves the wave equation by using a finite difference method to reach its results. In this method, the pile is divided up into springs, masses and dashpots of about 1 meter long. Furthermore, detailed information about the hammer and driving system, and the soil can be given as input for the solving of the wave equation.

FEM models have also been made to analyze stress concentrations for pile driving. [47] [48] In other research [48] a numerical study of pile driving dynamics, using the finite element method is presented. The aim of this research was to obtain a numerical solution which could closely represent the true behaviour of idealised problems. This research argues that a fine mesh is required to obtain an accurate representation of the propagation of the impact wave from the hammer.

The research concludes by saying "A new one-dimensional pile driving model, consisting of a one-dimensional pile is shown to give results which agree very closely with those obtained by accurate finite element analysis. Comparisons are made with published examples of pile driving analysis, and the new one-dimensional model is found to be more accurate than these previous finite element analyses." [48] The Finite Element Method produces accurate results, but at the time of the referenced study, it was easier to use the traditional analytical analysis

In other research, [47] a typical three-dimensional six-pile group is analyzed and compared with results from other computer programs for pile group analysis that are based on different approaches. This method is used to analyze field and laboratory tests of piles, and is shown to be in good general agreement with the computed data. This is an excellent example of the Finite Element Method being used in a scenario for pile analysis where analytical results are harder to come by, and FEM is a good alternative.

Furthermore, in other research the frequently used GRLWEAP software is compared to a FEM analysis and drivability results from an existing wind farm, concluding a close resemblance. [49] Although these Finite Element Models are anticipated to enhance the precision of predictions, they involve high computational costs. As a result, they were never able to replace the initial model. However, for perforated monopiles, they seem to be the only viable comparison, as there are no analytical models (yet) for these perforated structures.

1.5. Research gap

From this literature review, it can be concluded that a clear knowledge gap is visible. Perforated monopiles are a promising technology for the development of offshore wind farms in intermediate water depth, but due to their novelty little is known about how they are to be installed. There is no literature available on how the perforated monopile is to be installed. There is a fear that the stresses that occur during hammering will increase beyond what would be considered acceptable in terms of fatigue damage. The perforations will cause the wave force introduced by the hammer to travel through smaller areas. Sending the same amount of force through a smaller area is expected to enhance stress concentrations.

Furthermore, the curvatures of the perforations may also cause stress concentrations as a result of the wave force being redirected due to the presence of these perforations. A final cause of concern is the reduction in the efficiency of installation. The perforations may absorb some of the hammer impact by deforming, which will reduce the amount of force that is used for penetration into the soil. This means more blows are required for the installation of these perforated monopiles. This will both increase installation time and fatigue damage. All of these concerns will produce unknown changes in the fatigue damage due to hammering, which will need to be analyzed before the perforated monopile can be used.

This thesis aims to perform a drivability study for a perforated monopile, similar to the studies done for a regular monopile. For the perforated monopile, no method exists yet to perform a drivability study. As there is no analytical model available to perform this drivability study, a new FEM model has to be built from scratch, which has to be subjected to load cases representing the hammering of the perforated monopile.

1.6. Research questions

In order to perform a drivability study of the perforated monopile and to fill the knowledge gap explained in the previous section, a main research question, as well as several sub-questions are devised. For this thesis, the main research question is as follows:

> Do perforations limit installation of monopiles via hammering, and if so, by how much?

To help answer this main research question, the following sub-questions are formulated:

- What are the stresses for non-perforated monopiles during installation, and how do we determine fatigue damage?
- What are the stresses for perforated monopiles during installation?
- How much of the energy from the hammer impact is lost due to the perforations in the monopile?
- What is the fatigue damage for the installation of perforated monopiles?
- What changes can we make to the hammer and the perforated monopile to improve installation performance?

These research questions will determine the drivability of perforated monopiles and fill the existing knowledge gap. This will be achieved by analysing the stress concentrations and the interpretation of what this means for the fatigue damage during hammering. In the coming chapter, it will be analyzed how these research questions are to be answered.

2 Methodology

Now the research gap and the research objectives have been determined, a plan of action has been developped that can be used to fill the research gap. In this chapter, the key parameters of the monopile, perforations, soil, and hammer force will be introduced and developed in the following chapters.

2.1. Thesis approach

This thesis can be divided into 3 phases that aim to answer the research questions posed in the previous section, followed by a discussion of the results and a recommendation for possibilities for future research.

2.1.1. Phase 1: Fatigue damage during installation of non-perforated monopiles

The first phase of the thesis will look at the installation of non-perforated monopiles in 80 meter water depth, and the fatigue damage associated with this installation. The geometries of the non-perforated monopile will be defined based on the previous research on perforated monopiles [35], which is in turn based on the standard model of a 15 MW wind turbine. [50] The bottom outer diameter is 13.1m, with an embedded length of 52.4m and a wall thickness of 82 mm. A conical section with a 4.5 degree angle is included to transition from the wider area, starting at 40 meters above the mud-line up to 59.7 meters where the diameter is reduced to 10 meters with a wall thickness of 62 mm. During this conical section, a constant wall thickness of 72 mm is chosen. The monopile continues for 35.3 more meters, on top of which the tower is placed. For a more detailed description see figure 3.1 in chapter 3.

The monopile has been recreated in both Ansys, a FEM program, to look at stress concentrations, and in GRLWEAP, a program specialized in determining drivability. The Soil Resistance to Driving (SRD) has been determined based on previous research [51], which looks at soil conditions that are to be expected in the deeper parts of the North Sea. The soil consists of two layers of clay on top of a layer of sand, which extends to 52.4 meters of embedded length, details of which can be found in table 3.2 in chapter 3.

Furthermore, the load cases that are introduced by impact hammering are also introduced. The IHC-S-4000 impact hammer is used, which, according to the manufacturer, is sufficiently sized for this monopile. [52]. The force loads are based on previous research [53] [54], and the GRLWEAP software, which also provides a graph of the force over time due to the hammer impact. The force is applied as a distributed load on the top area of the monopile. All the inputs of soil, monopile, and hammer, are used in the GRLWEAP software to determine stress concentrations and drivability. The results from this part will be compared to literature in chapter 3 to verify whether the model can also be used for perforated monopiles.

2.1.2. Phase 2: Fatigue damage during installation of perforated monopiles

After this phase, the perforated models used in previous research [35] are recreated in Ansys. Since the perforated model can not be recreated in GRLWEAP, only Ansys is used. The model is slightly simplified so that it is easier to compute and focus is placed on the perforations. The monopile around

the waterline remains the same: 35.3 meters in length, a diameter of 10 meters with a wall thickness of 62 mm. The conical and bottom parts are replaced with a 30m extension, with the same properties. This is done to simplify the model, the validity is explained in section 4.3. Perforations are introduced by creating new smaller cylinders and subtracting these from the base structure, as can be seen in figure 2.1. The steps are as follows:

(a) the creation of the first cylinders
(b) the first cylinders are rotated by 60 degrees
(c) the first three rows of cylinders are created, all rotated 60 degrees with respect to each other
(d) the cylinders are scaled with a factor of 3.1/1.6 to create elliptical cylinders according to geometry 2, explained in chapter 4
(e) the elliptical cylinders are subtracted from the main cylinder
(f) the process is repeated for the other 2 rows, which are rotated 30 degrees to the other perforations

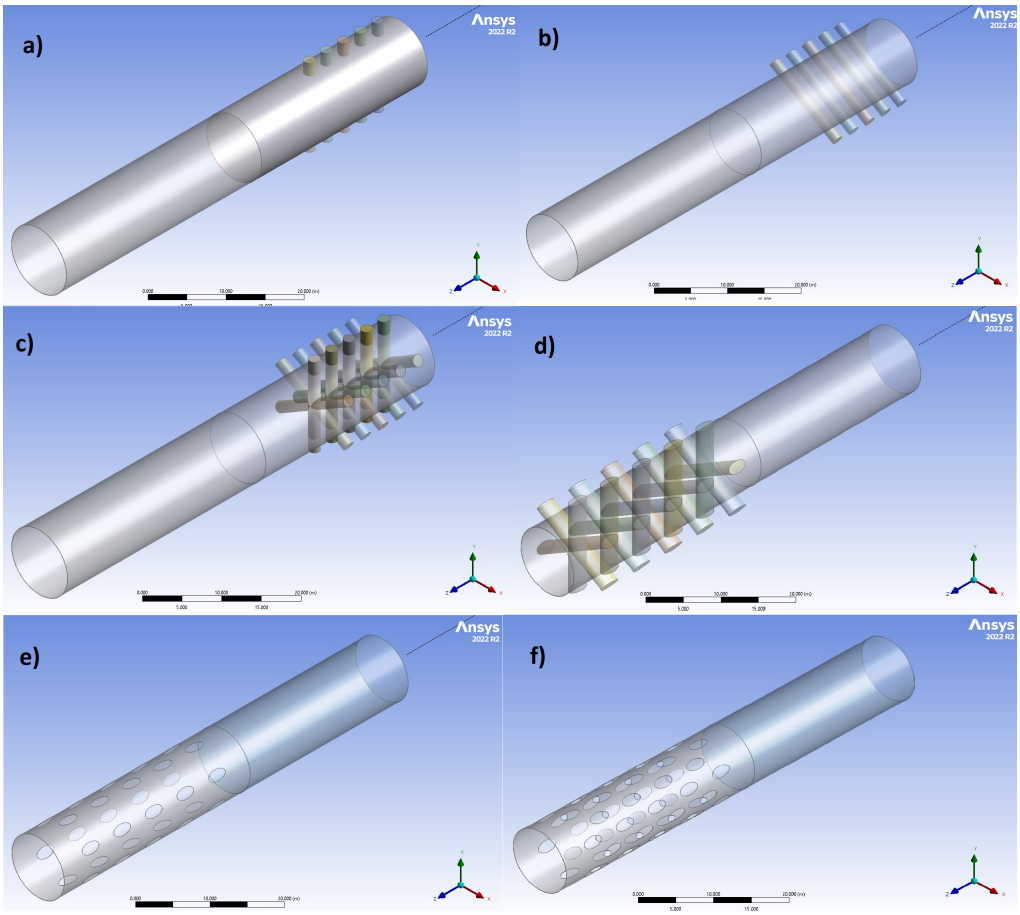

Figure 2.1: The introduction of the perforations in monopile in Ansys in 6 steps, according to the dimensions from geometry 2, explained in chapter 4, and fixed to the bottom

Of main interest in this phase are the stress concentrations and the potential loss of energy due to the perforations. The loss of energy will be calculated based on the reaction force at the bottom and on the velocity, as per the following formula, also used in previous research [53]:

$$E = \int_0^{\Delta t} F_i v_i dt \tag{2.1}$$

Using these inputs it will be reviewed whether or not pile driving is possible in a similar manner as it is for a regular, non-perforated monopile. The bottom of the monopile is fixed, and can't move.

2.1.3. Phase 3: Optimizing

The third and final phase revolves around improving the pile driving for perforated monopiles. Drawing from the conclusions that can be made from the first two phases an attempt is made to come up with a solution that maximizes the reduction in area affected by hydrodynamic loading around the waterline, and minimizes fatigue damage due to installation. This has been attempted by making changes in the layout and dimensions of the perforations, and by making changes in the loads.

From the research during the previous phases it can be concluded that ellipses provide a lower stress concentration compared to circles. As such, the height of the perforations can be increased, whilst maintaining the width, in an attempt to lower the stress concentrations, whilst maintaining a high reduction in area. Two versions of such a dimension are analyzed in section 5.3.1.

For the different loads, a vibro-hammer is used, as well as a reduction in loads by the impact hammer. According to the theory described in formula 3.3 in section 3.4 the fatigue damage is dependent by a third order on the stress concentrations, and linearly on the blow count. By reducing the hammer load, and by using a vibratory hammer, the stresses are lowered, but the blow count is increased. In section 5.3.3 and 5.3.2 it is analyzed that this reduces the fatigue damage by a factor of approximately $\frac{\sqrt{2}}{2}$ and 2 for the reduced hammer load and the vibro-hammer respectively.

2.2. Software used

In this thesis, a diverse range of software tools is employed to conduct the necessary analyses and calculations for addressing the research questions. The following section provides an overview of all the software utilized, along with version information.

2.2.1. GRLWEAP 14

GRLWEAP, short for ”Wave Equation Analysis of Piles,” is a software program used for the analysis of pile driving dynamics. It is primarily employed in geotechnical and civil engineering for predicting the behaviour of piles during installation. GRLWEAP is based on the wave equation method, which models the pile-soil interaction during driving. The software helps engineers simulate and analyze the stresses, forces, and displacements experienced by piles as they are driven into the ground. This information is crucial for assessing the suitability of different pile types, determining the required pile lengths, and optimizing the pile-driving process to ensure the structural integrity and stability of the foundation.

The wave equation used in pile driving analysis is typically derived from principles of wave mechanics and soil dynamics. The one-dimensional wave equation for pile driving can be expressed as:

$$A\frac{\partial^2 p}{\partial t^2} + B\frac{\partial p}{\partial t} = C\frac{\partial^2 u}{\partial x^2} \tag{2.2}$$

Here:

- p is the pile dynamic resistance,
- u is the pile displacement as a function of time and depth
- t is time
- x is depth
- A, B and C are the coefficients that depend on the pile and soil properties

In GRLWEAP, pile material of steel can be selected, and the pile can be divided up into various sections, with various wall thicknesses, starting with a straight section around the waterline, then a conical section, and then again a straight section, which is driven into the soil. GRLWEAP divides the pile into segments of approximately 1 meter in length, to be used for the wave equation, which models these segments as masses connected in a mass/spring/dash-pot system.

The soil can be used as an input either from rough soil description and classification, or SPT-N values, density and friction angles. In this study however the soil properties were known, and customized soil

parameters were used as an input. The shaft resistance and toe resistance are the most important input parameters, but the full list of parameters used in this study can be found in figure A.2 in Appendix A.

Furthermore, in GRLWEAP there is a database of properties from certain hammers, including the IHC-S-4000, the main hammer used in this research. The ram weight used is 1,976 kN, and the maximum energy is 3,998 kJ. A helmet weight of 161 kN was used, a drop height of 2.02m, and a rather arbitrary efficiency of 83%. The GRLWEAP program uses the manufacturer's recommended driving system to develop these parameters into a graph of force over time.

GRLWEAP combines this information on pile, soil, and hammer, and uses it to solve wave equation 2.2. This wave equation uses force and resistance, as a mass/spring/dash-pot system, to determine the displacement of the monopile and the stresses over the pile.

GRLWEAP 14 was kindly provided free of charge in the version of a free university license.

2.2.2. Ansys Workbench 2022 R2

ANSYS Mechanical is a finite element analysis (FEA) software package developed by ANSYS, Inc. FEA is a numerical technique for finding solutions to physical problems by dividing a complex structure or system into smaller, simpler parts (finite elements) and analyzing the behaviour of these elements. In this thesis, the monopile will be divided into 'solid' elements, as can be seen in figure 2.2. Various sizes of the elements are tried, ranging from 0.2 to 2 meters. For the bottom part of the model, the 'sweep method' is used, which results in a large height and a small width of each element. This helps create a representative model with fewer elements, as the height along the simplified model is assumed not to influence the wave propagation, but the width, especially around the monopiles, does influence the stress concentrations.

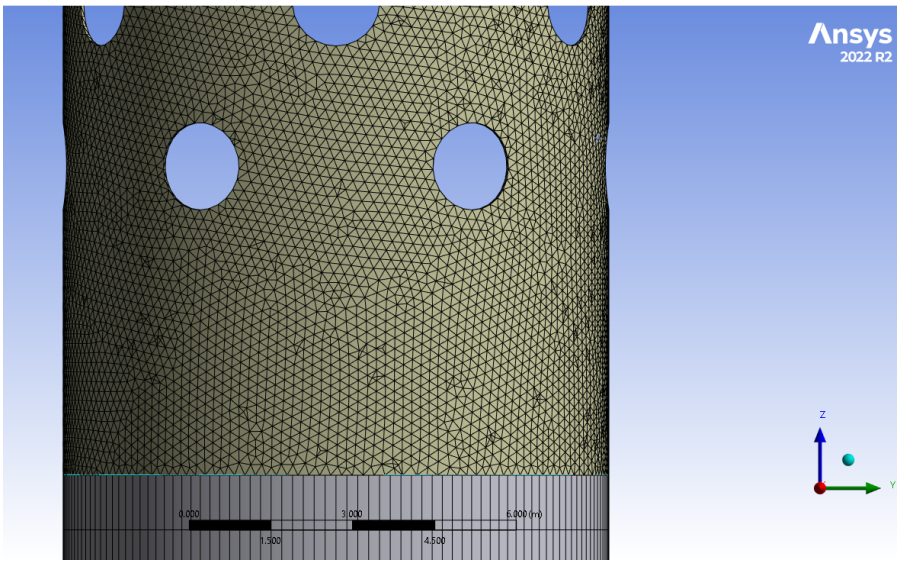

Figure 2.2: Close up of the smallest mesh used for geometry 1, using elements of size 0.2 meters

The small elements are set up as PDEs (Partial Differential Equations), similar to equation 2.2 and the model in figure 1.9, but in three dimensions. The continuous PDEs are transformed into a discrete form to make them suitable for numerical solution. Furthermore, the hammer force is introduced at the top of the monopile, and to determine the reaction force, the bottom of the monopile is fixed. The explicit solver directly solves the system of equations for each time step without iterative processes.

For the explicit dynamics calculations, Ansys uses a 'Central difference' method. [55] After forces have been computed at the nodes of the mesh (resulting from the hammer impact or the boundary condition of the fixed bottom), the accelerations per node are derived by using Newton's second law, equating

acceleration to force divided by mass. The accelerations are:

$$\ddot{x}_i = \frac{F_i}{m} + b_i \tag{2.3}$$

where

- $\ddot{x}_i$ are the components of nodal acceleration (i=1,2,3; the directions)
- F_i are the forces acting on the nodal points, in this case due to the impact hammer, in direction i
- m is the mass attributed to the node
- b_i are the components of body acceleration

With the accelerations at a specific time n determined, the velocities at time $n + \frac{1}{2}$ are found from

$$\dot{x}_i^{n+\frac{1}{2}} = \dot{x}_i^{n-\frac{1}{2}} + \ddot{x}_i^n \Delta t^n \tag{2.4}$$

and finally, the positions are updated to time n+1 by integrating the velocities

$$x_i^{n+1} = x_i^n + \dot{x}_i^{n+\frac{1}{2}} \Delta t^{n+\frac{1}{2}} \tag{2.5}$$

For time steps, the user-defined input of the force is input with steps of 0.1 milliseconds. To determine the inner time steps in the Ansys program, the CFL (Courant-Friedrichs-Lewy) condition is used to check for stability. This condition relates the time step size to the mesh size and material properties, as can be seen in the formula below:

$$C = \frac{u\Delta t}{\Delta x} \leq C_{max} \tag{2.6}$$

where u is the velocity, Δt is the time-step, and Δx is length interval. Furthermore, a time step safety factor of 0.9 is used, and ANSYS employs automatic time step adjustment algorithms to adapt the time step during the simulation based on the evolving characteristics of the solution.

Ansys is available free of charge for TU Delft students.

2.2.3. Microsoft Excel 2019

A widely recognized and flexible software package that provides capabilities for various tasks, including multiparameter calculations, data ordering, and plotting. In the context of this thesis, its primary use revolves around organizing and storing data and probe results from the Ansys and creating figures.

2.2.4. MATLAB R2023b

MATLAB is a high-level programming language primarily used for numerical computing, data analysis, and visualization. MATLAB provides a comprehensive set of tools for tasks such as algorithm development, data analysis, modelling, and simulation. In this thesis, MATLAB is used to determine the force over time generated by the impact hammer in Appendix A, based on the analytical models from previous research [54].

2.2.5. Overleaf

Finally, Overleaf is used as a cloud-based LaTeXeditor for the writing and editing of this thesis.

3

Installation of a non-perforated monopile

This thesis aims to determine if stress concentrations during hammering of perforated monopiles limit installation via hammering. To do so we will look at the stress concentrations during hammering. At first a non-perforated monopile Finite Element Method (FEM) model will be created in Ansys. In order to make an accurate determination of the fatigue damage a proper representation of the hammer force must be made, as well as a careful representation of the soil properties. Once the stresses and number of hammer blows are known, a determination of the fatigue damage can be made. After this, the fatigue damage is compared to readily available literature and software (GRLWEAP) available for drivability analyses to determine the validity of the FEM model.

3.1. Reference monopile

To determine the stress concentrations a Finite Element Model of the monopiles from previous research is recreated in Ansys. [35] This regards a 15 MW reference turbine in a water depth of 80 metres. The monopile has a constant D/t ratio of 160. The bottom diameter is 13.1 m, resulting in an embedded length of 52.4 m. Additionally, a conical section with a 4.5 degree angle is included to transition from the wider area, starting at 40 meters above the mud-line up to 59.7 meters where the diameter is reduced to 10 meters. During this conical section, a constant wall thickness of 72 mm is chosen. The monopile continues for 35.3 more meters, on top of which the tower is placed. The tower starts with a diameter of 10 meters and a thickness of 4.8 mm, is 138 meters long and at the top is 6.5 meters in diameter with a thickness of 3 mm. On top is placed a point mass of 1017 tonnes to resemble the rotor nacelle assembly (RNA). Further details of the tower structure can be found in the research defining this monopile. [50] A simple sketch of the tower can be seen in figure 3.1

Parameter	Symbol	Value	Units
Young's modulus	E	2.00E11	Pa
Shear modulus	G	7.93E10	Pa
Density	ρ	7.85E3	kg/m^3

Table 3.1: Material properties of the tower

In Ansys structural steel is selected as a material choice. The material properties of the steel used for the monopile can be found in table 3.1. For the installation, it is assumed that the tower will be installed later. For this paper only focus is placed on the monopile itself, marked in red in figure 3.1. The bottom of the monopile is assumed to be fixed to the ground.

3.2. Hammer force

Installation vessels for offshore monopiles are either jack-ups that stand firmly on the seabed during installation or motion-compensated crane vessels. From this position, a crane lifts a monopile into

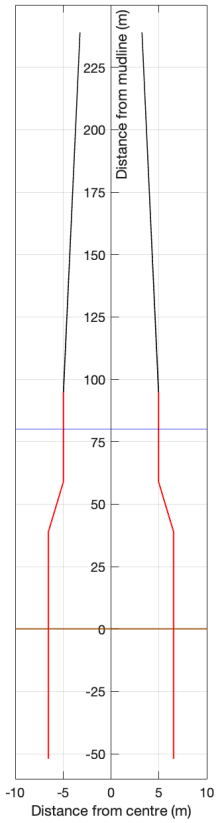

Figure 3.1: Monopile dimensions [35]

place. The monopile is kept in place by pile-handling tools like gripper devices, while the monopile is driven into the sea floor. [29] There is interesting research being done into the gentle driving of piles, but for now nearly all of the monopiles are driven into the seabed hydraulically to reach the desired penetration depth. [36] In this section it will be analyzed which hammer is suitable for the installation of a 10m diameter monopile, and what the force over time looks like.

3.2.1. Perikleous et al.

To determine the drivability and hammer forces for the monopile described in the previous section, a reference is made to the drivability analysis performed by G. Perikleous et al., which focused on energy losses during driving. [53] In this research, a comparison is made of an Abaqus model created by the research, with the measured forces at the installation of a monopile at the HOW01 windfarm site of Ørsted (formerly Dong Energy) in the UK, finding strong overlap in their findings.

In this research, a hydraulic impact hammer IHC-S4000 with a rated energy of 3998.2 kJ was utilized. The force measured and calculated over time in this research can be seen in figure 3.2. It is important to note that the energy of 1,100 kJ measured in the research is significantly lower than the maximum setting of the IHC-S-4000, which is 4,000 kJ.

According to the manufacturer this hammer can be used for most 10 metre diameter piles, and that in some specific cases, the IHC-S-5500 will be needed. [52] Because of the availability of data for the S-4000, this hammer is also used in the analysis performed in this thesis.

3.2.2. Deeks and Randolph

Furthermore, the force from above also correlates with the standard work by Deeks and Randolph from 1993, which provides a force wave overtime at the pile head. [54] This paper presents an analytical

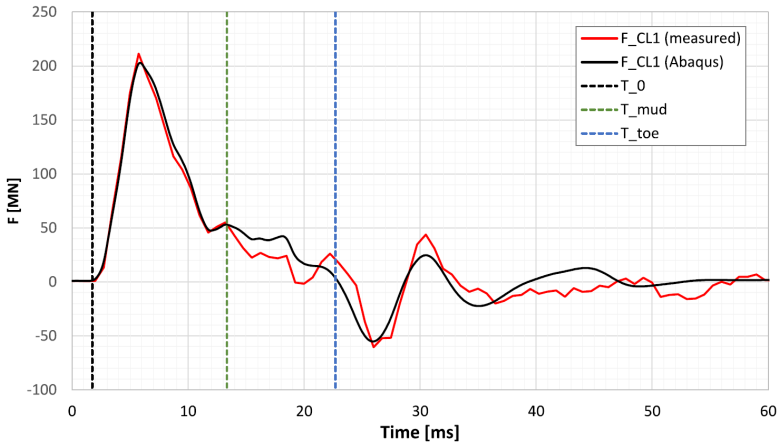

Figure 3.2: Force signal of IHC-S4000 as measured in previous research [53]

model of the hammer impact based on lumped ram and anvil masses separated by a cushion with internal damping, connected to the pile, which is modeled as a dashpot. [54] The work provides a force wave at the pile head based on an analytical model of hammer impact, based on lumped ram and anvil masses, separated by a cushion with internal damping.

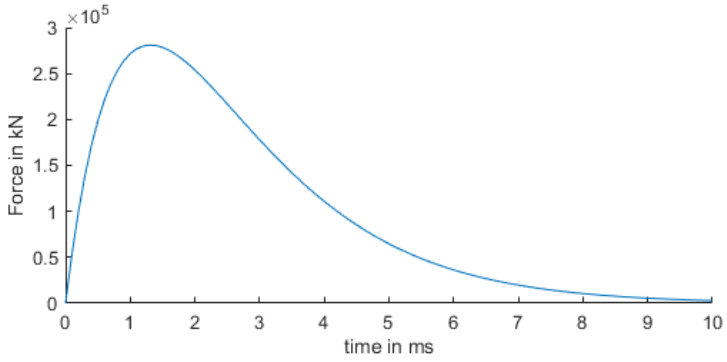

Figure 3.3: Force signal of IHC-S4000 as determined based on previous analytical work [54] See the source code in Appendix A

The research is recreated using the known parameters from the IHC-S-4000, taken from GRLWEAP, and the parameters of the monopile. The results of the analysis for the force over time can be seen in figure 3.3. The governing formula to determine this graph is shown in equation 3.1 and the calculations and the source code can be seen in Appendix A. The work does not seem to take into account the possible reflections of the force that occur within the hammer itself, and so provides a rather smooth graph of the force over time compared to the measured results.

$$f_p = EA/c_p \cdot e^{-\frac{k_c^*}{2} t^*} \tag{3.1}$$

3.2.3. GRLWEAP

Finally, the GRLWEAP program also provides the force of the IHC-S4000 hammer as a function of time, depending on the characteristics of the input, like drop height and efficiency. Using a drop height of 2 meters and a (rather arbitrary) efficiency of 83%, the force generated by the GRLWEAP program shows a strong correlation with the characteristics of the other two works cited in this section [54] [53]

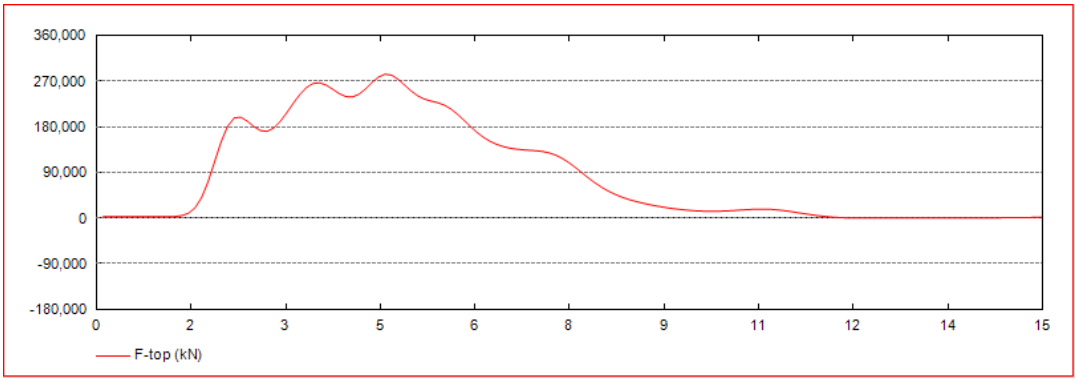

Figure 3.4: Force signal of IHC-S4000 generated by GRLWEAP per millisecond

The analytical calculations provide a smoother flow of the force over time, whereas the GRLWEAP graph has some bumps in the graph. It is assumed that these are caused by the reflections of the wave force in the hammer itself, which dissipate over time. Furthermore, the peak in force in figure 3.2 is slightly lower compared to the other two graphs, implying that a lower drop height is used during the hammering process. This can also be deduced from the energy of 1,100 kJ measured in the same paper, which is much lower compared to the maximum energy available for the IHC-S-4000.

The GRLWEAP program then goes on to use this input force to determine stresses, drivability, and blow count, as will be discussed in the next sections. To make a valid comparison between the GRLWEAP and the FEM model, the force generated by GRLWEAP will be used as an input for the FEM model. In the FEM model, the load will be applied as a 'remote force' applied evenly on the top edge of the monopile. The force as a function of time can be seen in figure 3.4.

3.3. Resistance to Driving

To determine drivability, first, the Soil Resistance to Driving (SRD) is determined. This SRD is used to determine the amount of hammer blows required and to determine the maximum compressive and tensile stresses in the pile. These stresses and blow counts are combined to estimate the fatigue damage. [41][42]

The SRD is typically derived by adjusting the calculation used to determine the ultimate static axial pile capacity in compression. In literature two research papers [43] [41], along with design codes [44] [45] [26][46] provide excellent design guidelines for determining fatigue damage and pile drivability, including calculations for the Stress Concentration Factor (SCF). [46] Unfortunately, most of these methods to determine SRD are based on smaller diameter piles that are used for offshore oil & gas platforms. "It is important to note that to date an SRD methodology specifically tailored to monopiles such as the ones used in the Offshore Wind industry is yet to be developed." [56]

More recently, research has provided public insight into the drivability of large-diameter piles. [51] In this paper, a 7.8m diameter monopile is installed by hammering. The soil analyzed there consists of two clay layers on top of a sand layer, whose properties can be found in table 3.2 on the next page. These soil properties show similarity to other soils, like those analyzed in other research [57], which also has a shaft resistance varying between 5 and 50 MPa, depending on penetration depth.

The SRD consists of the 'shaft resistance', which accumulates as a larger part of the shaft is embedded into the soil, and of the 'toe resistance', which is the bottom area of the monopile multiplied with the resistance pressure present at the embedded depth. The full input data for the GRLWEAP software can also be seen in figure A.2 in Appendix A.

Using this data as input, the SRD is computed, a prediction for the blow count is made, and this is compared to actual results measured during installation. The results of the SRD analysis are verified

Parameter	Clay A	Clay B	Sand
Depth [m]	0-18	18-27	27-42
Description	Fissured firm to hard silty slightly micaceous CLAY	Stiff to hard sandy silty CLAY	Silty clayey fine to medium SAND
Bulk density [Mg/m^3]	1.93	2.1	2.01
Water content [%]	34	24	27
Plasticity index [%]	92	27	-
Particle size, d_{10} [mm]	-	-	0.006-0.06
Undrained strength (UU) [kPa]	178	151	-
Relative density [%]	-	-	100
Peak friction angle [°]	-	-	38
Remoulded strength [kPa]	166	85	-
Residual friction angle [°]	9	21	31
G_{max} P-S logging [MPa]	100-200	180-320	200-600

Table 3.2: Soil properties at installation location [51]

in the GRLWEAP software and used for the larger model from this thesis. This results in the SRD that can be seen in figure 3.5. The graph shows an increase in resistance along the shaft as the penetration depth increases, with several peaks caused by local increases in toe resistance, specifically around 30 and 36 meters of penetration, as is also highlighted in figure A.2 in Appendix A. This SRD results in the total number of blows of 4178 at full force required to drive the pile to the desired depth of 52.4m. These blows use a drop height of 2 meters and an efficiency of 83%

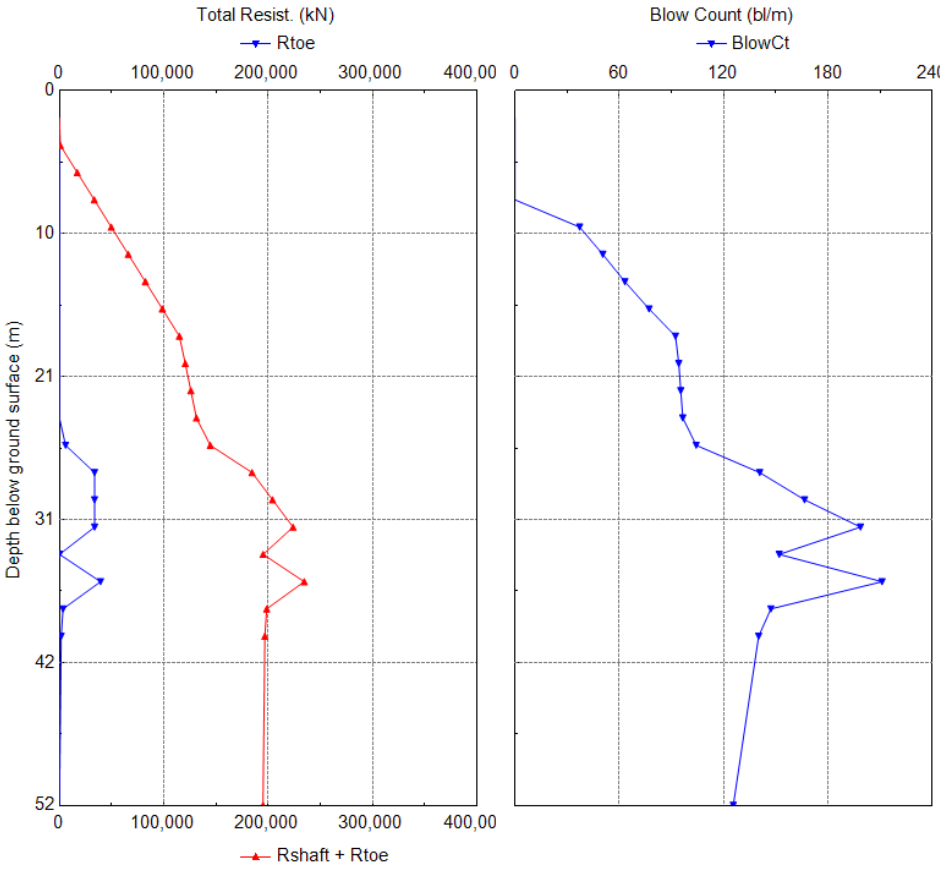

Figure 3.5: SRD for the non-perforated monopile from this thesis

It was assumed that the soil properties of the bottom sand layer could be extended from the original depth of 42 meters up to the desired penetration depth of 52.4 meters for the desired penetration depth of the larger pile analyzed here. Altering the properties of the shaft and toe resistance of the bottom sand layer only showed a minor influence on the total blow count. Even an increase of the shaft resistance up to 100 kPa resulted in only an increase of less than 10% of the total blow count.

3.4. Fatigue damage

Previous research [41] states that cumulative fatigue damage D is evaluated with the Palmgren-Miner rule:

$$D = \sum_{n=i}^{\infty} \frac{n_i}{N_i} \tag{3.2}$$

with N_i = number of cycles before failure occurs for a given stress ratio variation $\Delta\sigma_i$, and n_i = number of cycles inflicted to the structure for the $\Delta\sigma_i$ stress variation. The design guideline provides guidance on the fatigue design of offshore steel structures and more precisely on the calculation of the stress concentration factors to be adopted in fatigue analysis. [46] This design guideline also provides S-N fatigue curves.

The design guideline cited is used for high-cycle loading (defined as more than 10,000 loadings), but can also be linearly extrapolated to fewer cycles for practical use in fatigue assessment. [46] Furthermore, the recommended practice is valid for stainless steel up to 550 MPa. The guideline is also used in other research [58] to determine fatigue damage due to installation. DNV is a globally recognized classification society and DNV standards, such as DNV-RP-C203, are widely accepted and respected in the industry, and are also used for larger diameter monopiles.

The basic design S-N curve is given as

$$log_{10}N = log_{10}\overline{a} - m \cdot log_{10}(\Delta\sigma(\frac{t}{t_{ref}})^k \tag{3.3}$$

with the values for $\overline{a}, m, t, t_{ref}$ and k given in table 2-1, 2-2, and 2-3 of the design guideline cited. [46] The research cited provides a case study where the fatigue damage on a 6 m diameter and 48 m length monopile is analyzed, as it has been driven up to 26.25 m into the soil. [58] In this example case the fatigue damage for the whole length of the monopile is assessed. Here instead only the highest stress concentrations are analyzed, as this will be the governing case.

To determine the fatigue damage, the stresses during installation are computed. GRLWEAP provides maximum tensile (T.) and compressive (C.) stresses during hammering along the height of the monopile. They are calculated by the following formula:

$$\sigma = \frac{F}{A} \tag{3.4}$$

where σ is the compressive or tensile stress, F is the force, and A is the cross-sectional area.

Compressive and tensile stresses are very useful for the one-dimensional wave equation that is being solved by the GRLWEAP program. The compressive stresses are the highest, being 148.0 MPa at the top of the monopile, and 151.2 MPa at the start of the conical section, as can be seen in the middle of figure 3.6 on the next page. Snapshots from the relevant timestamps in the Ansys software are shown further below in figure 3.7, which also shows the relevant locations of the stress concentrations at these timestamps.

Ansys generates a maximum von Mises stress over time, which can be seen in the right of figure 3.6. Four snapshots at the relevant times also show the propagation of the stress wave through the monopile, and the location of the stress concentrations measured can be seen in figure 3.7. Von Mises stress is a way of combining the individual stresses in a material to assess the potential for yielding or failure.

$$\sigma_{\mathsf{VM}} = \sqrt{\frac{1}{2}\left[(\sigma_x - \sigma_y)^2 + (\sigma_y - \sigma_z)^2 + (\sigma_z - \sigma_x)^2\right] + 3\tau_{xy}^2 + 3\tau_{yz}^2 + 3\tau_{zx}^2} \tag{3.5}$$

where

- σ_x, σ_y and σ_z are the normal stresses in the x, y, and z directions, respectively.
- τ_{xy}, τ_{yz} and τ_{zx} are the shear stresses on the xy, yz, and zx planes, respectively.

.
The von Mises stress is useful because it provides a single scalar value that represents the equivalent stress of a complex three-dimensional stress state. The first peak, at 5 ms and 159.6 MPa, is at the top of the monopile and corresponds to the hammer reaching its peak force. The second peak is reached at 12ms at 152.6 MPa and corresponds to the force reaching the start of the conical section. Due to the close similarity of the stresses it is safe to say that in this aspect the models are verified and valid. To determine the fatigue damage, the average of the middle 2 stresses is taken, which corresponds with a stress of 151.9 MPa at the start of the conical section.

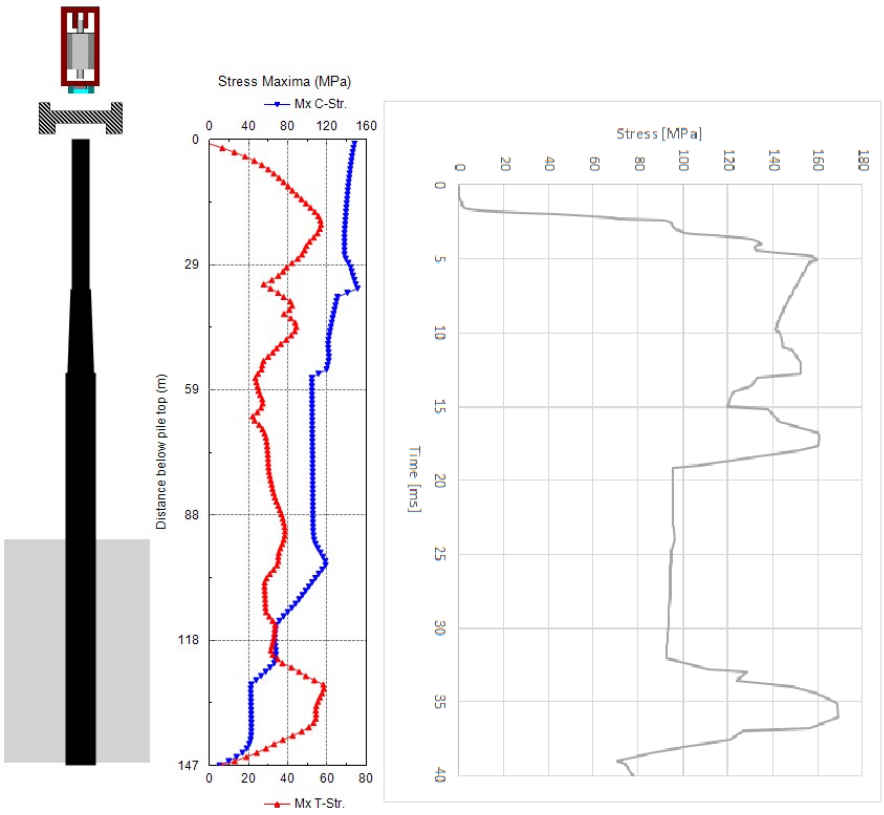

Figure 3.6: Stresses along the height of the monopile due to hammering. The GRLWEAP graph is shown in the middle, the graph on the right is from Ansys results

There are 2 other peaks in Ansys, shown in figure 3.6 and 3.7, that do not correlate with the peaks from GRLWEAP. One peak at the 17 ms and 160.0 MPA, at the end of the conical section. The other peak is at 35 ms and 169.3 MPa, at the bottom of the monopile. These peaks are not considered for this analysis.

For simplicity purposes, the Ansys model does not include all possible sources of damping, like water, that are present in real life, and presumably also in the GRLWEAP program. Research has shown that that the presence of water can cause significant losses in energy, and thus stresses, that are beyond the scope of this thesis. [49] In short, the stress waves very briefly compress the monopile, and also the water inside of it whilst travelling downwards. The compression of this water in the conical section is found to use up approximately 35 % of the energy in the hammer blow. As such, the real experience stresses at the end of the conical section and at the bottom are assumed to be smaller than the stresses at the top of the monopile and at the start of the conical section.

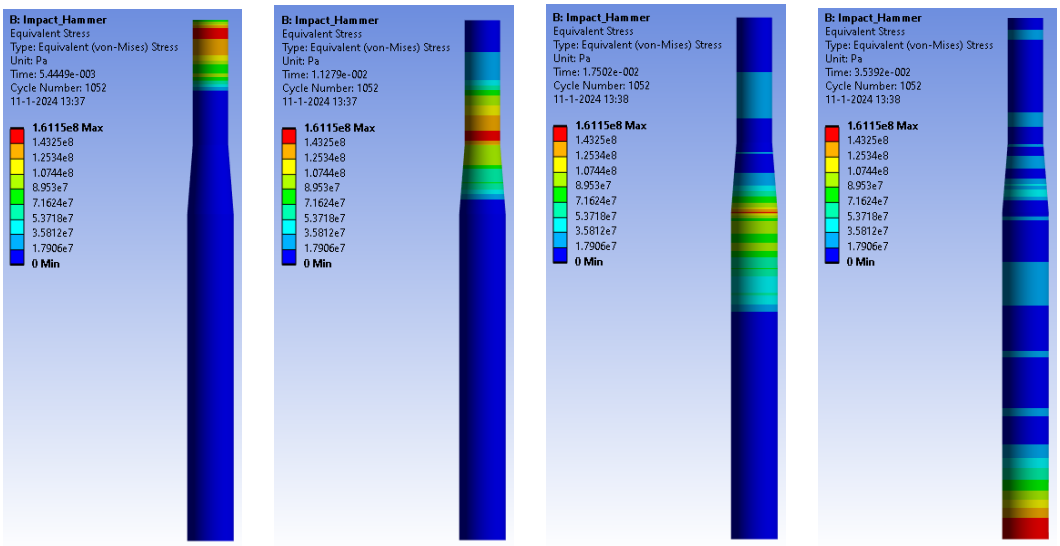

(a) Peak 1 at 5 ms at the top of the pile

(b) Peak 2 at 11 ms, 35m from the top

(c) Peak 3 at 18 ms, 55m from the top

(d) Peak 4 at 35 ms at the bottom of the pile

Figure 3.7: Stress concentrations along the height of the monopile at the relevant time steps

Furthermore, the stresses at the bottom of the monopile are assumed to be caused by the bottom being completely fixed and thus immovable. In reality, and in the GRLWEAP program, some of the energy is already lost due to resistance in the water and the soil, and the bottom of the monopile is displaced slightly and gives way, thereby reducing stress concentrations. In the Ansys model, such considerations are not taken into account as they are beyond the scope of this research. As such, in the Ansys model, the full force and energy of the impact hammer is transferred and reflected at the bottom, causing an unusually high-stress concentration there.

Unless otherwise indicated, detail category C1 is used, as described in the design guideline. [46] Given a stress range of 151.9 MPa, a maximum of $3.19 \cdot 10^5$ blows can be used before the fatigue limit is reached. As there are only 4178 blows required for instalment, a fatigue damage of 1.31% is applied.

At the location of the welds, the stress range needs to be multiplied by a Stress Concentration Factor. Assuming an SCF of 1.55, the maximum number of blows decreases to $8.58 \cdot 10^4$ and the fatigue damage increases to 4.87%. This SCF is based on the highest SCF from other research and is considered the governing case.[58]

3.5. Summary and results

In this chapter the dimensions and properties of the monopile are defined, which are based on the model of a 15 MW turbine monopile foundation. [50] The hammer force is also introduced. The standard analytical work [54] provides a good basis but fails to include the reflected force wave within the hammer itself. Hence, the results from the GRLWEAP program are used, which correlate strongly with the measured results from other research [57] as shown in section 3.2. Using the force from the GRLWEAP program, with a peak of 275 MN, also ensures similarity in comparing the resulting stress concentrations.

The force causes stress concentrations at both the top of the monopile and at the start of the conical section, with stress concentrations of 148 and 160 MPa respectively according to the GRLWEAP software. The peaks in Ansys at these points are of similar magnitude: 160 MPa and 153 MPa at the top of the monopile and at the start of the conical section respectively, as can be seen in figure 3.6. These stresses are multiplied by a factor of 1.55 to take into account stress concentrations caused by butt welds, as explained the research cited. [58].

The Soil Resistance to Driving is taken from recent research [51], which provides public insight into the drivability of large monopiles and shows similarity with the soil analyzed in other cases [57]. The soil properties are used and translated to an SRD for the larger monopile from this thesis. The SRD consists of shaft resistance, which increases with driving depth, and toe resistance, which depends only on the toe area and on the soil properties at a specific depth. This SRD, with a peak of approximately 200 MN of resistance, is used as an input into the GRLWEAP program.

GRLWEAP combines this information on pile, soil and hammer, and uses it to solve the wave equation. This wave equation uses force and resistance, as a mass/spring/dash-pot system, to determine displacement of the monopile, and the stresses over the pile, from which a blow count is computed. This blow count is then used to determine fatigue damage according to the design guideline. [46] Using a stress concentration factor of 1.55 this results in a total fatigue damage of 4.87%.

4

Installation of a perforated monopile

Now that the FEM model has been verified in the previous chapter, it's time to look at what the stress concentrations at the perforated monopile are. Furthermore, it must also be determined how much of the hammer force is actually transferred to the bottom of the monopile, compared to the non-perforated monopile. There is a fear that some of the force may be absorbed by the perforations, which could increase both stresses at the perforations, and the amount of blows required to reach the desired penetration depth. In this chapter, the drivability analysis of the perforated monopile will be performed.

4.1. Ansys model

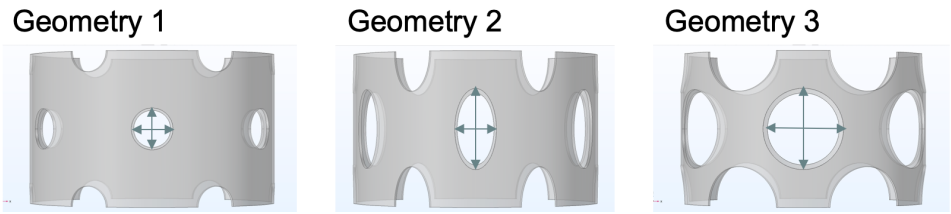

Figure 4.1: The three perforation geometries that are analysed in previous research [35]

In the previous chapter it was discussed that stress concentrations occur at the top of the monopile and at the start of the conical section. For the perforated monopile stress concentrations are expected around the perforations. To save on computing power, only the perforated part is recreated in Ansys. The perforated part is 35.3 meters in length and has an outside diameter of 10 meters with a wall thickness of 62 mm.

-	Geometry 1	Geometry 2	Geometry 3
width [m]	1.6	1.6	3.1
height [m]	1.6	3.1	3.1
β [%]	12.9	24.8	48.6

Table 4.1: Geometry dimension, where β is the reduced area

The research from before analyzed three different geometries for the perforations, which will all be analyzed here. [35] The dimensions of these perforations can be seen in table 4.1 and figure 4.1. The perforations are distanced by 60 degrees, in such a way that there are 5 layers of 6 perforations spaced over the diameter of the monopile. Another 4 layers of perforations are present that are located in between the 5 previously mentioned layers. These are rotated 30 degrees compared to the other 5 layers. An overview of this can be seen in figure 4.2. The perforations are produced in Ansys by creating cylinders with the appropriate dimensions, and by subtracting these cylinders from the larger

monopile. For geometry 2, cylinders are created with a radius of 0.8 meters, which is then scaled in the z-direction, to create elliptic cylinders with a width of 1.6 meters and a height of 3.1 meters. An overview of how this is achieved in Ansys can be seen in figure 2.1 in chapter 2. The hammer force from the previous section is again introduced, and the bottom of the monopile is again fixed.

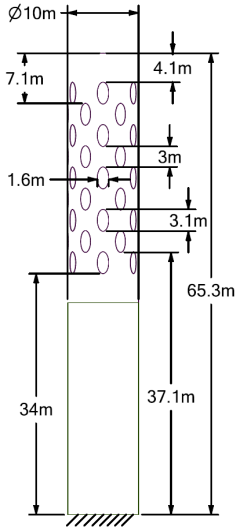

Figure 4.2: The full dimensions of the simplified model for geometry 2. Other geometries use the same centre points for each perforation, with different width and height

4.2. Stress concentrations

The stress concentrations are analyzed by an explicit dynamics analysis in Ansys. As can be seen in figures 4.3 and 4.4, the stresses at the perforations are highest at the sides of the ellipses for geometry 2.

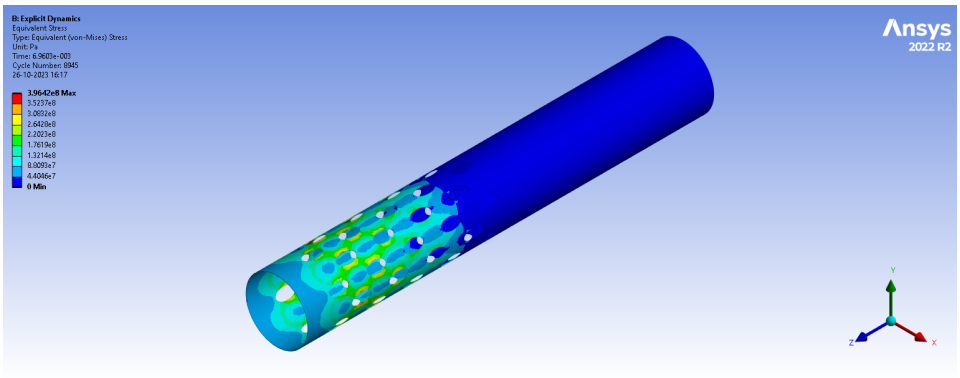

Figure 4.3: The stresses for geometry 2 as computed by Ansys for a mesh size of 0.5 meters at 7 milli-seconds

The stresses are also highest at the sides of the perforations of geometry 1 and 3. There was no significant difference in the stress concentrations for the different rows or columns affected by the hammer force within the same geometry monopile. Stress concentrations are again observed when the force wave reaches the bottom of the monopile, due to it being fixed there. However, these stress concentrations are not assumed to be representative of the actual situation during installation, as in reality, these forces will dissipate into the perforations, water, and soil, which is now not modelled adequately.

The mesh convergence for geometry 2 can be seen in figure A.3, which shows a less than 2% difference in peak stresses between an element size of 0.5m and 0.2m, showing the convergence of the results. Geometry 1 and 3 reach a peak of 435 and 853 MPa respectively, as can be seen in figure 4.5. So far geometry 2 looks the most promising, both in terms of stress concentrations and reduced area. The

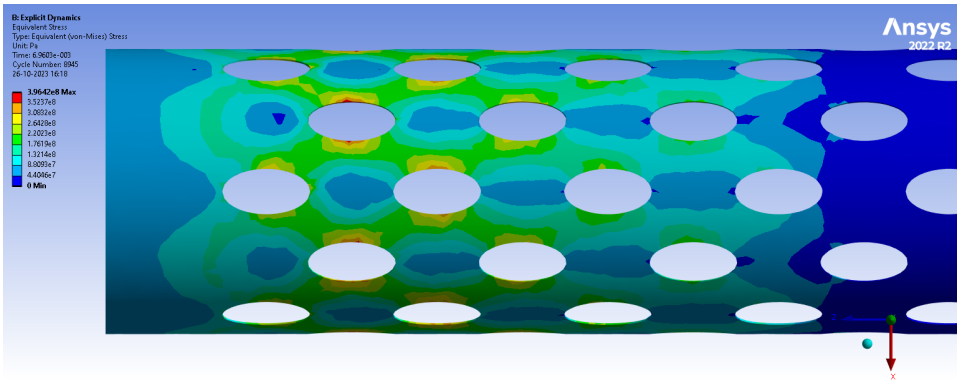

Figure 4.4: A close-up of the stresses for geometry as computed by Ansys for a mesh size of 0.5 meters at 7 milli-seconds.

stress concentrations for geometry 1 and 2 have more than doubled compared to the non-perforated monopile. The stress concentrations for geometry 3 are increased nearly 5-fold.

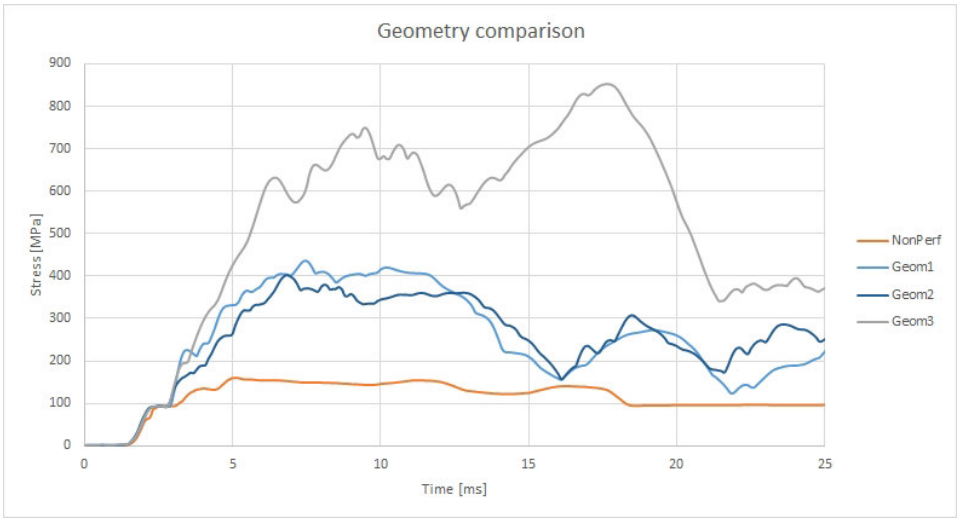

Figure 4.5: The stress concentrations for various geometries over time

4.3. Force throughput

As mentioned before, in order to determine if the blow count is the same for both the perforated and the non-perforated monopile, it is important to analyze if the full force of the hammer blow is passed on through to the bottom of the monopile. Research [53] shows significant driving losses were occurring due to the conical section of a non-perforated monopile. Analyzing such losses lies beyond the scope of this paper. As such, again, only the top part of the monopile is recreated, both with perforations and without. To determine how much of the force is passed on to the bottom a probe is placed on the bottom of the monopile and the reaction force is measured. If the perforations absorb some of the force introduced by the hammer, there will be less force throughput and the reaction force will be lower there. There will also be a velocity probe placed just below the perforations, in order to measure the velocity of the displacement at this position.

The force travels like a wave through the monopile and is bounced back up by the fixed bottom of the monopile. A figure of the force travelling through the pile can be seen in Appendix A. This wave travels back to the top of the monopile where again it is bounced back to the bottom. This process continues until all energy of the force is dissipated, e.g. via losses in the perforations or in the water and soil. In the model not all losses, like those through the water and soil, are taken into account, as this is beyond

the scope of this paper, and the only interests for now are the losses due to the perforations. As such, again, only the top part of the monopile is recreated.

To prevent the double measuring of the reflected wave the straight section of the monopile is extended with 30 meters, so the full hammer force reaches the bottom of the monopile before the first part of the hammer force is measured twice. The 30 meter distance is chosen based on the velocity of the force in steel, which is approximately 5.000 m/s, and on the time required for the hammer impact force to fully develop, which is around 12 milliseconds. This means the force will travel 60 meters in the time it takes for the hammer force to fully develop, so up and down the 30 meter distance of the extension.

This ensures that the full reaction force can be measured before the reflected wave can have an impact on either the velocity probe or on the stress concentrations around the perforations. This also allows the measurement of the velocity after the perforations, as the velocity would be impossible to measure if the monopile was fixed there.

In Ansys, a velocity probe was placed right after the perforated section, and 30m above the bottom of the model. The velocities of this probe are shown in figure 4.6. The order of magnitude of the velocity for all geometries is roughly the same, with only a small drop of around 9% for geometry 2. The delay in the velocity in geometry 3 however is notable.

This delay is probably due to the large size of the perforations present in geometry 3. The force wave needs to pass through a much smaller area, continuously being bounced off of the perforations. This causes a delay and a somewhat spread in the results of the velocity and force reaction. Whilst the delay is indeed notable and large, it should be pointed out that this is only a delay in time, and the time step in between the peaks of the velocity and in reaction force is still the same as for the other geometries.

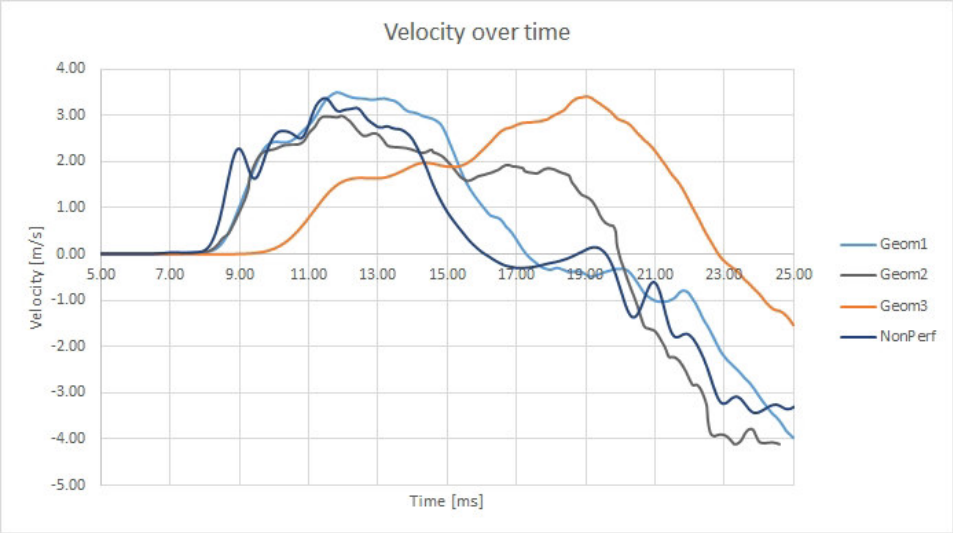

Figure 4.6: Velocity of the probe just below the perforations for all geometries in m/s

The velocity probe also confirms the reflection of the wave in approximately 12 ms, as can be seen in figure 4.6. For the non-perforated model and for geometry 1, at first, the velocity increases at around 8 ms, and the force travels through the velocity probe for approximately 9 ms. At 20 ms, the reflected wave arrives, and a negative velocity is observed. The same event is observed for the other geometries, with different time points. This confirms the 12 ms gap that the stress wave needs to travel 60 meters down and up the last part of the monopile.

The results of the reaction force are shown in figure 4.7 and table 4.2. As can be seen, the maximum reaction force is reduced by 13% for geometry 2 and 3. The reaction force for geometry 1 is only affected modestly. The mesh convergence for geometry 2 can be seen in figure A.4, which shows only

a small jump of 5% in reduction of the reaction force when the element size is reduced from 1m to 0.2m.

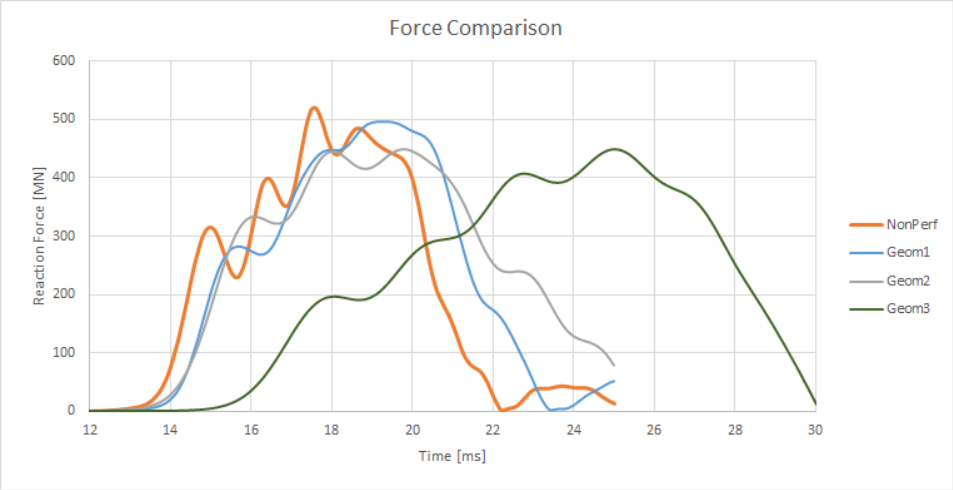

Figure 4.7: Reaction force at the bottom of the model for all geometries

Furthermore, the energy by the hammer, in accordance with previous research [53], is also linearly dependent on the velocity:

$$E = \int_0^{\Delta t} F_i v_i dt \tag{4.1}$$

Because the force can only be measured at a fixed point, it is measured at the bottom of the model, where the velocity is thus 0. Hence, the velocity is measured 30 meters above the fixed bottom, just beneath the perforations. To arrange for this discrepancy in measurements, only the peaks are looked at. The peak in velocity should correspond to the peak in reaction force. Combining these peaks should result in the maximum energy in the force wave induced by the impact hammer.

This suspicion is confirmed by looking at the time difference between the peaks. Force in a structure travels with the same speed as sound, which in steel is approximately 5,000 m/s. 6 milliseconds is just the right amount of time for the force wave to travel the 30 meters down the model to the fixed bottom. The peak in velocity occurs at around 11.5 ms for geometry 2 and the non-perforated model, and at 19 ms for geometry 3. The peak in reaction force occurs at around 18 ms for geometry 2 and the non-perforated model, and around 25 ms for geometry 3. For geometry 1 the peak in velocity is at 12.5 ms, and the peak in reaction force is at around 19 ms. These peaks are spaced approximately 6 ms from each other, confirming that it concerns the same parts of the wave that are analyzed and that the peak energy of all the waves across the different geometries are compared.

This reduced force and velocity is put back into the GRLWEAP model described in the previous chapter by lowering the drop height and efficiency in the GRLWEAP program. Reducing the force results in an increase in the blow count compared to the original blow count number of 4178. The increase in blow count per geometry is shown in table 4.2 on the next page.

4.4. Fatigue damage

The fatigue damage is assessed in a similar manner as for the non-perforated monopile in the previous section. The stress and blow counts and fatigue damage can be seen in table 4.2 on the next page. Again, an SCF of 1.55 and detail category C1 from table A-9 in the cited design guide is used. [46]

For the analysis of the fatigue damage for geometry 1, if it is possible for the perforations not to cross the circumferential butt welds that are present in the monopile, detail category B1 can be used, and no SCF would be necessary. This would result in a fatigue damage of just 31.8%.

-	Non-perforated	Geometry 1	Geometry 2	Geometry 3
β [%]	0	12.9	24.8	48.6
Reaction force [MN]	519	497	449	451
Velocity [m/s]	3.45	3.44	3.17	3.41
Number of blows [-]	4178	4303	5063	4711
Stress [MPa]	159	435	405	853
Fatigue Damage [%]	4.87	117.8	111.9	973.3

Table 4.2: Reduced area β, maximum reaction force, velocity, stress concentrations, required blows and fatigue damage for the different geometries analyzed.

4.5. Summary and results

In this chapter, the model is recreated in Ansys based on the dimensions from the previous research cited. [34] [35] The model is slightly simplified in order to save on computing power and to focus on the stress concentrations around the perforations, making sure to maintain the validity of the model. The non-perforated model is also recreated and simplified, showing the same stress concentrations for both models, see figure 3.6 and the same peaks at 5 ms in figure 4.5. This shows that the stress concentrations do not depend on the length of the rest of the model.

The reaction force is measured at the bottom of the model, and the velocity is measured just after the perforations, 30 meters from the bottom of the model. The reaction force for geometry 1 is roughly the same as for the non-perforated model with the same dimensions. For geometry 2 and 3 there is a drop in the reaction force of 13.5% and 13.3% respectively.

The velocity and the reaction force are reduced slightly due to the perforations. Geometry 1 and 3 show a very minor decrease in its velocity, whereas geometry 2 reduces the velocity of the probe by 8.1%. Do note the reversal of the velocity, which starts roughly 12 milliseconds after the start of the displacement of the velocity probe for the non-perforated model, as well as for geometry 1 and 2. This is expected to be because of the reflection of the force wave at the bottom of the model. Force in a structure travels with the same speed as sound, which in steel is approximately 5,000 m/s. 12 milliseconds is just the right amount of time for the force wave to travel up and down the extension of 30 meters.

For geometry 3 there is a significant delay in the reaction force and the velocity of the probe located 30 meters from the bottom of the model, just after the perforations. The force wave needs to pass through significant holes that can cause deflections of the wave, which can cause this delay. The curvatures and the reduction in area due to the perforations are the cause of significant stress concentrations.

Geometry 1 has only a negligent effect on the loss of energy, with an increase of 3.0% in blow count, whereas geometry 2 and 3 require an increase in the blow count of 21.2% and 12.8% respectively. For geometry 1 it is assumed that the force wave can pass through the structure relatively unhampered since the perforations are small with respect to the area of the monopile. For geometry 2 and 3 the force wave needs to find a way past all the perforations before reaching the velocity probe and the bottom of the model, where the reaction force is reached.

From the stress concentrations, it can be concluded that the perforations have a significant impact on the stresses present in the monopile. Even the relatively small perforations present in geometry 1 cause a more than doubling of the stress concentrations. This also causes a significant increase in fatigue damage: a two-fold increase in stress causes a 2^3, or an 8-fold increase in fatigue damage. The loss of energy has only a small effect on the fatigue damage. A 21.2% increase in blow count only results in a 21.2% increase in fatigue damage.

The total fatigue damage summarized in table 4.2 shows that no monopile can be installed using the IHC-S-4000 with the current settings. If it is possible to create geometry 1 without having the perforations cross the butt-welds, this would generate a fatigue damage of 31.8%.

5

Conclusion and possible alternatives

The primary goal of this study was to compare the perforated monopile vs the non-perforated monopile, in terms of drivability. Furthermore, the secondary goal was defined as coming up with possible alternatives for driving a perforated monopile, such as using a different type of hammer or making alterations in the dimensions of the perforations. These two topics will be addressed in this chapter.

5.1. Model comparison

The non-perforated model has been created in both Ansys and GRLWEAP, where both models showed much similarity. The perforated model unfortunately could not be recreated in the GRLWEAP software, and could only be recreated in Ansys. The non-perforated model had a structured mesh, with rectangular solid elements along the height of the monopile. The perforated monopile used the same rectangular elements where possible but used triangular elements where necessary to account for the holes present in the monopile. A mesh refinement was performed where the smallest step used were mesh elements of size 0.2 meters. Ansys uses solid elements, nearly all of which are tetrahedral, with a small amount of hexahedral mesh elements used.

5.1.1. Stress comparison

The stress ranges for the Ansys model and the GRLWEAP model of the non-perforated monopile show great similarity and concurs with literature cited. [58] The largest stresses occur at the top of the monopile and at the start of the conical section. The stress concentrations at the end of the conical sections and at the bottom of the monopile are assumed to be lower compared and are beyond the scope of this thesis.

Furthermore, monopiles consist of multiple shorter sections that are welded together using butt welding. This means detail category C-1 from the design guide line table A-9 is to be used. [46] At the location of the welds, the stress range needs to be multiplied by a Stress Concentration Factor. Assuming an SCF of 1.55. This SCF is based on the highest SCF from other research in this area, and is considered the governing case.[58]

The results of the perforated monopile showed a significant increase in stresses due to the width of the perforations. It is interesting to note that the differences in stresses between geometry 1 and 2 are very small and that geometry 1 shows an even slightly higher stress concentration around the perforation, despite having the same width in the perforations, and a lower height. The stress concentrations are highest at the sides of the perforations in the case of all geometries, as can be seen in figure 4.4 for geometry 2.

For geometry 3 the stress concentrations were beyond any limit of what could be considered acceptable for installation purposes. Even not taking into account a possible stress concentration factor due to welds, the fatigue damage inflicted upon the structure was above 300%. Using an SCF of 1.55 and taking into account butt-welds will result in a ten-fold exceedance of the fatigue damage, not even considering the ultimate limit state.

As mentioned, detail category C-1 is used, as the stress concentrations are expected around the butt-welds. For geometry 1, it should be possible for the perforations to not coincide with the butt-welds. Hence, detail category B1 from table A-9 from the design guideline [46] can be used, which would result in a lower fatigue damage of 28.1%, which amounts to a reduction in fatigue damage with a factor of 4. For geometry 2 and 3, it would be impossible to avoid the butt welds because of the size of the perforations.

The stress concentrations seem to arise from several factors. At first, the area through which the force has to travel is reduced in the perforated monopiles. The same force divided over a smaller area causes higher stresses. Furthermore, the curvatures can also cause stress concentrations, as they redirect the force wave that is propagating through the structure. This means that a possible optimization of the perforations to reduce fatigue damage will have to take these factors into account. As the reduction in area is partly the goal of these perforations, the most logical place to look for in terms of optimization would be the reduction in curvatures.

Besides the reduction in curvatures, care should also be taken so as to avoid having high-stress concentrations around the butt-welds. As can be seen from the fatigue damage calculation for geometry 1, the presence of these butt-welds around the perforations can cause a four-fold increase in fatigue damage due to installation.

A final point to look into is to decrease the hammer force, which will also reduce the stress concentrations. As mentioned, a two-fold increase in stress causes a 2^3, or an 8-fold increase in fatigue damage. Halving the hammer force would thus also reduce the fatigue damage by a factor of 8. In the next section, it will be analyzed what this could potentially mean for the blow count.

5.1.2. Blow count

After determining the stress concentrations, it is important to determine the blow count. The blow count for a non-perforated monopile was determined to be 4,178, using the GRLWEAP software as shown in chapter 3. Furthermore, the energy by the hammer, in accordance with relevant literature [53], is linearly dependent on both the velocity and the force:

$$E = \int_0^{\Delta t} F_i v_i dt \tag{5.1}$$

As such, both the force and velocity are analyzed. The velocity is analyzed just after the perforations, or 30 meters from the bottom of the model. The reaction force is analyzed at the bottom of the monopile, where it is fixed to the bottom. For both of these parameters, they decreased after the introduction of the perforations. Because the force travels downwards as a wave through the monopile, it is expected that this wave will be bounced off of the perforations, which can cause both a reduction in force and in speed. Furthermore, the deformations in the steel around the perforations can also be responsible for a part of the loss of energy. This results in a loss of energy that can be seen in table 5.1

-	Non-perforated	Geometry 1	Geometry 2	Geometry 3
Reaction force [MN]	519	497	449	451
Velocity [m/s]	3.45	3.44	3.17	3.41
Energy losses [%]	-	3.4	20.5	14.2
Number of blows [-]	4178	4303	5063	4711
Stress [MPa]	159	435	405	853
Fatigue Damage [%]	4.87	117.8	111.9	973.3

Table 5.1: Parameters and results for the different geometries analyzed.

This reduced energy is used as an input in the GRLWEAP software. In this software, the same non-perforated pile is used (because the perforated pile isn't possible), and the input energy is simply reduced, by reducing drop height and the efficiency until the desired loss is reached. This reduced energy

input is used to determine the new blow count according to the wave equation used in the GRLWEAP program. The result is an almost linear relationship between reduced input and increased blow count.

It is important to note that this only looks at the increased blow count, resulting in increased fatigue damage. There are other drawbacks, such as increased installation time, that accompany this increased blow count, which could also be considered a serious downside due to the introduction of the perforations. However, compared to the increase in stress concentrations, the blow count has only a minor impact on the fatigue damage.

5.1.3. Fatigue damage

After having determined the blow count and the stresses, the fatigue damage can be analyzed and compared. The full analysis can be seen in chapters 3.4 and 4.4 and is largely reliant on the deisgn guideline cited. [46] As can be seen, this fatigue damage is largely dependent on the stress ranges. The blow count does play a small, linear role in the fatigue damage. The stress concentration, however, plays a third-order role in determining the fatigue damage: a two-fold increase in stress causes a 2^3, or 8-fold increase in fatigue damage. From table 5.1 it can be concluded that both geometry 1 and 2 are viable alternatives to the traditional non-perforated monopile, but geometry 2 has the overwhelming preference, as this has a much larger reduction in area, and thus a reduction in hydrodynamic loading, as confirmed by previous research. [35]. Still, none of these monopiles can be installed without exceeding fatigue life of the structures.

These calculations do assume a detail category C1 for all models. Using the same stress concentrations and blow counts, but detail category B1 for geometry 1 and 2 results in a cumulative fatigue damage of 31.8% and 28.1% respectively. This emphasizes the reduction available if butt-welds can be avoided around the perforations.

5.2. Research questions

This research started with the main research question:

> Do perforations limit installation of monopiles via hammering, and if so, by how much?

To help answer this main research question, the following sub-questions are formulated, which will be addressed in this section:

1. What are the stresses for non-perforated monopiles during installation, and how do we determine fatigue damage?
2. What are the stresses for perforated monopiles during installation?
3. How much of the energy from the hammer impact is lost due to the perforations in the monopile?
4. What is the fatigue damage for the installation of perforated monopiles?
5. What changes can we make to the hammer and the perforated monopile to improve installation performance?

The final subquestion will be addressed in section 5.3, and the main research question will be answered in the discussion in section 6.1

5.2.1. Non-perforated monopiles

- *What are the stresses for non-perforated monopiles during installation, and how do we determine fatigue damage?*

In chapter 3 the first sub-question is answered by looking at previous research [58] and by recreating the monopile in GRLWEAP and Ansys. The stresses are approximately 152 MPa, which has to be increased by a stress concentration factor of 1.55. The blow count is determined in the GRLWEAP software, by using the dimensions of the monopile, the parameters of the impact hammer, and the properties from the soil into account, and solving the wave equation, from earlier research [37]. The wave equation divides the pile into a large mass/spring/dashpot system, with the soil as resistance, and in this case, resulting in a blow count of 4,178. Using the design guideline cited [46], the fatigue damage reaches nearly 5%, as can be seen in section 3.4

5.2.2. Perforated monopiles

- *What are the stresses for perforated monopiles during installation?*

For the perforated monopiles, the stresses increased significantly, up to 435, 405 and 853 MPa for geometry 1, 2 and 3 respectively. The stresses need to be multiplied by an SCF of 1.55 as explained in section 4.5. The stress occurs at the side of the perforations, where the remaining surface area over which to divide the force is the smallest. The circular perforations of geometry 1 lead to a slightly higher stress concentration compared to geometry 2 with elliptical perforations, presumably due to the sharper edges.

5.2.3. Energy losses

- *How much of the energy from the hammer impact is lost due to the perforations in the monopile?*

The loss in energy is dependent on the size of the perforations and is 3.4%, 20.5% and 14.2% for geometry 1, 2 and 3 respectively. This is based on the energy equation, based linearly on force and velocity, described in section 5.1.2. For the determination of the loss of energy, only the maximum values of the reaction force and the velocity were taken into account.

5.2.4. Fatigue damage

- *What is the fatigue damage for the installation of perforated monopiles?*

The fatigue damage is determined in subsections 3.4 and 4.4, and summarized above in section 5.1.3. The fatigue damage for installation is 117.8%, 111.9% and 973% for geometry 1, 2 and 3 respectively, compared to a fatigue damage of nearly 5% for the non-perforated monopile. Hence, none of the geometries can be installed. If the perforations can avoid the butt-welds geometry 1 and 2 have a fatigue damage of 31.8% and 28.1% respectively, and can thus be installed.

5.3. Possible alternatives

Now most of the research questions have been answered, it is time to look at the final sub-question:

- *What changes can we make to the hammer and the perforated monopile to improve installation performance?*

What are the possible alternatives that can keep the fatigue damage due to installation as low as possible, whilst maintaining a large reduction in area affected by the hydrodynamic loading? Taking lessons from the results and conclusions presented in the previous section an attempt will be made to reduce the curvature of the perforations and to change the loads applied on the top of the monopile, in the following subsections:

- Geometries
- Vibrohammer
- Reduced force

5.3.1. Geometries

Different geometries were analyzed for stress concentrations using the same impact hammer IHC-S-4000 as before. Using the results from before, elliptical shapes were preferred above circular shapes. Furthermore, an attempt was made to create larger holes to reduce hydrodynamic loading even further. Pictures of the geometries tried can be found in figure 5.1, and the results of the stress concentrations can be found in table 5.2.

Geometry 4 used six large holes. Six large boxes were created, with a width of 2.6m, and a height of 21.7m. At both ends, semi-ellipses were created, with a width of 2.6m, and a height of 3.9m. This was then subtracted from the monopile. Geometry 5 uses a similar layout to geometry 2 but uses fewer and higher holes. The height of the holes is doubled to 6.2m, keeping the same width of 1.6m. Only 3 perforations are placed above each other, as opposed to 5 in geometry 2. Geometry 5 has the same dimensions as recent research into the reduction of hydrodynamic loads. [59]

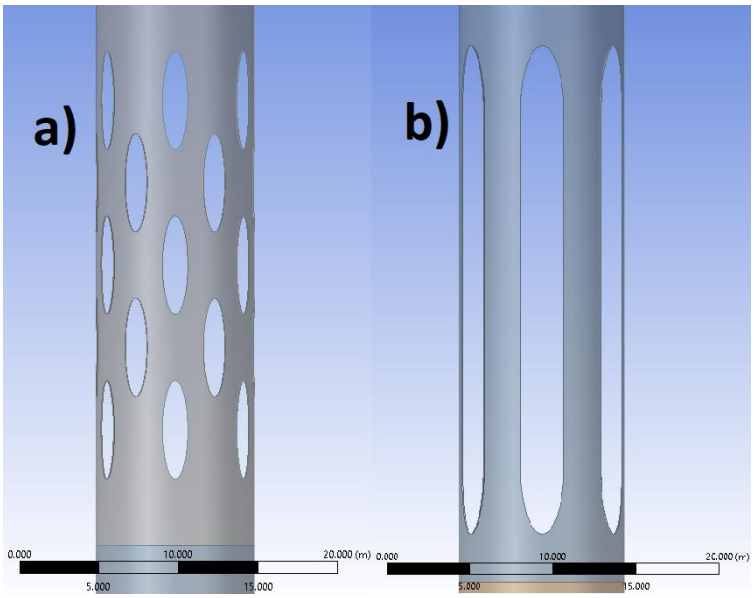

Figure 5.1: Geometry 4 (b) and 5 (a)

As can be seen in table 5.2, the velocity of the probe just after the perforations increases for both geometry 4 and 5. It is assumed this is the case because the wave of the force is funnelled through the smaller section that is left after the perforations are introduced. Because the same amount of force and energy has to go through a smaller area, the force and velocity are assumed to increase.

-	Non-perforated	Geometry 4	Geometry 5
β [%]	0	47.3	26.8
Reaction force [MN]	519	562	468
Velocity [m/s]	3.45	4.88	3.95
Number of blows [-]	4178	-	-
Stress [MPa]	159	337	312
Fatigue Damage [%]	4.87	53.2	42.2

Table 5.2: Reduced area β, stress concentrations, required blows and fatigue damage for the different geometries analyzed.

For the determination of the fatigue damage, it is assumed that the same amount of blows are required for full penetration as for the non-perforated model. Furthermore, due to the size of the perforations, it is assumed that the butt-welds are present at the perforations. Hence, the worst-case stress concentration factor of 1.55, and detail category C1 from table A-9 from the design guideline are used [46]. This results in the fatigue damage that can be seen in table 5.2. If butt welds can be avoided, using detail category B1 and no SCF, the fatigue damage is 6.52% and 4.79% for geometry 4 and 5 respectively. It is also important to note that this analysis only investigates fatigue damage, and other failure modes like buckling are not analyzed.

5.3.2. Vibratory hammer

Vibratory pile driving is a method whereby the monopile is vibrated into the soil, rather than being hammered in. The feasibility of instalment using a vibratory hammer is now analyzed, for both the non-perforated monopile and for the perforated ones. Use is again made of the GRLWEAP program, which also contains various vibratory hammers. The biggest vibratory hammer available is QU-CV640, which is also used for the monopile from this thesis. Unfortunately, after 28 meters of penetration, pile refusal occurs in the software. For reference, the IHC-S-4000 impact hammer requires 1255 blows to reach the same depth of 28 meters.

Since there is no easy alternative available, both the installation of the perforated and non-perforated monopiles are compared using both the vibratory and the 'normal' hammer up until 28m of penetration. GRLWEAP again provides a graph of the force over time exerted by the vibrohammer and, using the same soil profile as before, the QU-CV640 hammer requires 3 minutes before the 28m mark is reached. The vibrohammer, using an efficiency of 90%, generates a sinusoidal-like wave with peaks of +80MN and -65MN and a period of 43 ms.

For the non-perforated model, this corresponds to 4,186 blows with a maximum stress concentration of 70.1 MPa. The results for the other geometries, obtained in a similar manner as for the impact hammer, can be seen in table 5.3. The loss in energy is again implemented in the GRLWEAP program by reducing the efficiency in relation to the loss in energy. This reduced efficiency is then used to determine the new duration of pile driving, which is translated into the new blowcount. For geometry 3 however, the loss of energy was too high and pile refusal occurred. The fatigue damage for the other geometries is calculated according to table 2.2 from the design guideline [46], using detail category C1 for all geometries and SCF 1.55.

-	Non-perforated	Geometry 1	Geometry 2	Geometry 3
Reaction force [MN]	168.1	144.5	158.2	79.1
Velocity [m/s]	0.92	0.87	0.80	0.61
Energy losses [%]	-	26.5	26.3	71.9
Number of blows [-]	4186	6977	6977	N/A
Stress [MPa]	70.1	115.4	88.7	122.6
Fatigue damage vibro-hammer [%]	0.48	3.57	1.62	N/A
Fatigue damage impact hammer [%]	1.46	35.4	33.6	292.4

Table 5.3: Parameters and results for the different geometries analyzed for the vibrohammer QU-CV640 with penetration up to 28m.

As can be seen in table 5.3, the increase in stresses is much less compared to the impact hammer, with stresses increasing by a factor of 1.65, 1.27 and 1.75 for geometry 1, 2 and 3 respectively with the vibrohammer, as opposed to a factor of 2.74, 2.55 and 5.36 for the impact hammer. As such, the fatigue damage is much lower for the use of the vibrohammer. It is important to note, however, that the vibrohammer was only able to install the pile up to a depth of 28 meters. The impact hammer only required 1,255 blows for the same penetration. Still, taking this into account, the vibrohammer only uses up half of the fatigue damage that otherwise would be used up by the impact hammer.

5.3.3. Reduction in hammer force

As mentioned, the reduction in stress concentrations plays a cubic role in fatigue damage. If the stress concentration can be halved, the fatigue damage is reduced by a factor of 2^3, or 8 times. This will increase the amount of blows required, and thus installation time, but will also significantly lower fatigue damage. In this subsection, the efficiency of the impact hammer will be halved, from 83% to 41.5%, reducing the input energy to 1,600 kJ. The graph of the force over time can be seen in figure 5.2 on the next page.

As can be seen in figure 5.2, approximately 70% of the force remains when the energy input is halved. Because the energy is computed from equation 5.1, it is assumed that both the force and the velocity are decreased by a factor of $\sqrt{2}$, for a total reduction of a factor of 2.

This force is again used as an input in the simplified model in Ansys, where stress, velocity and reaction force are computed. The reaction force and velocity are again used to determine energy losses, and this is used as an input to determine the blow count required for installation. The fatigue damage is again calculated using an SCF of 1.55 and detail category C1 from the design guideline. [46] The results for all geometries, using a mesh size of 0.5 meters, can be seen in table 5.4

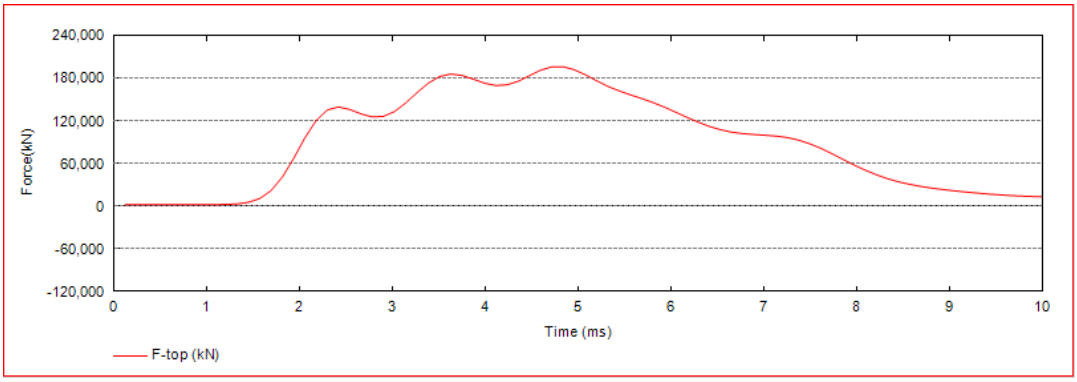

Figure 5.2: Hammer force over time, using an efficiency of 41.5%, as opposed to the efficiency of 83% used elsewhere in this thesis.

The stresses, velocities, and reaction forces over time for all these geometries can be found in Appendix B. Table 5.4 only shows the maximum values of these results. For geometry 4 and 5 the same blow count as for the non-perforated model is chosen, as it seems unlikely that the hammer energy, and thus penetration, can increase due to the presence of perforations.

-	Non-perforated	Geom 1	Geom 2	Geom 3	Geom 4	Geom 5
Reaction force [MN]	359	359	324	322	397	344
Velocity [m/s]	2.41	2.40	2.21	2.41	3.35	2.62
Number of blows [-]	7,668	7,699	9,265	8,549	7,668	7,668
Stress [MPa]	107	307	277	612	241	233
Fatigue Damage [%]	3.12	74.1	65.5	652	35.7	32.3

Table 5.4: Stress concentrations, required blows and fatigue damage for the different geometries analyzed with half the force.

From these results a clear reduction in fatigue damage is visible. The relative changes in reaction force, velocity and consequently blow count per geometry are similar as observed in table 5.1. The stress decreases linearly with a reduction in hammer force. Because the hammer force is reduced with a factor of approximately $\sqrt{2}$, so is the stress concentration. Because the stress concentration takes a cubed role in determining fatigue damage, this means the fatigue damage decreases with a factor of $\sqrt{2}^3$, or $2\sqrt{2}$.

However, because the input energy per blow is halved, approximately double the amount of blows are required to achieve full penetration. This increases the fatigue damage by a factor of 2, leaving behind a total fatigue damage that is approximately $\sqrt{2}$ lower than for the full hammer force. This can be confirmed when comparing the results in table 5.4 with tables 5.1 and 5.2. As can be seen in these results, the total fatigue damage is reduced by 34% on average, compared to the theory described above, which would have the fatigue damage reduced by 29%.

6

Discussion and recommendations

The results described in the previous chapter mean that the perforated monopiles with geometry 4 and 5 can be installed without exceeding the fatigue damage limit state. Geometry 1, 2 and 3 will not pass the fatigue limit state test for installation. The vibro-hammer looks promising to halve the fatigue damage but needs further research. Now the conclusion and results have been shown, a discussion of the results of the fatigue damage and this research is possible. Firstly, a critical look will be placed on this research. After this, recommendations for future research are made.

6.1. Discussion

As can be seen in section 5.3.3 in the results chapter, the fatigue damage is originally too high, but can be reduced to 32% by using geometry 5 and halving the input energy from the impact hammer. This is still significantly more than the 5% of fatigue damage for the non-perforated monopiles. The main research question was:

- *Do perforations limit installation of monopiles via hammering, and if so, by how much?*

From the research, we can conclude that not all types of perforations are possible and that the perforations limit the input energy to be used during hammering, thus increasing installation time.

Furthermore, the increased fatigue damage is certainly not to be underestimated. The main advantage of the use of a perforated monopile is the supposed *reduction* in fatigue damage. If the increase in fatigue damage due to installation undoes the reduction in fatigue damage due to reduced hydrodynamic loading, there is little to be gained from implementing the perforations. For geometry 2, previous research found a reduction in fatigue damage due to hydrodynamic loading of 32 percentage points for a water depth of 120m. [35] This means that unless a different installation method can be found, nearly all of the benefits of the perforations are undone by the increased fatigue damage due to installation.

It is possible that geometries and installation methods exist that improve the fatigue life of the structure, but this research was unable to find them. Combining a geometry similar to geometry 5 with a big enough vibro-hammer could prove to be a successful combination to reduce fatigue damage. Furthermore, for this research, it was assumed that due to the size of the perforations, the perforations will cross the butt-welds that are made to create the monopile. This required the use of an SCF of 1.55 and the usage of a more strict detail category, as explained in section 3.4 and 4.4. If it can be guaranteed that the perforations will avoid these butt-welds, this will also significantly reduce fatigue damage, for example by a factor of 4 for the case of geometry 1, as explained in section 4.4.

6.2. General recommendations

In this research, several assumptions were made, which will be analyzed here. These assumptions can be rechecked to optimize this research

6.2.1. Loss of energy due to perforations

In this research, the following energy definition is used, taken from previous research [53]:

$$E = \int_0^{\Delta t} F_i v_i dt \tag{6.1}$$

To determine the loss of energy the maximum velocity is taken just after the perforations, 30 meters from the bottom of the model. The reaction force is measured as the maximum force at the bottom of the model, as this is the only place possible to measure the force for Ansys. For none of the original geometries analyzed did these measurements significantly alter the total fatigue damage. For geometry 4 and 5 the total energy seemed to increase compared to the non-perforated model, which is hard to explain, and hence this can be expanded upon in future research.

Future research could look at a different way to measure the loss of energy, e.g. by measuring the force at the same place as the velocity probe, or by looking at the full time frame measured, and not just at the peak values. By using a different method to determine the conservation of energy, the blow count can either increase or decrease. This would change the results reached for the fatigue damage. It is important to note that the stresses have a third-order effect on the fatigue damage, and blow count only has a linear effect.

6.2.2. Simplified model

For the majority of the calculations in this thesis, the simplified model of a monopile is used. The analysis of the stresses elsewhere in the monopile was not the subject of this thesis. It is possible, however, that the perforations cause changes in the force wave travelling through the monopile, which may also alter the energy transferred to the soil, and thus the blow count.

It is known from other research [53] that the conical section can cause losses of up to 35% of energy for non-perforated monopiles. Future research could look further into the development of the force wave through the full monopile, including the conical section and potential losses in the water for the perforated monopile. If the amount of energy transferred into the soil reduces, this could increase blow count and fatigue damage. This could especially be the case for geometry 3, where the force wave is much more spread out than for other geometries. Furthermore, a smaller mesh could also provide a slightly different result.

6.3. Future research

Besides a critical look at this research, there are also plenty of options to expand on the research presented here, that can enable lower stress concentrations and thus lower fatigue damage. Three possibilities will be advised here:

- Other geometries
- Other loads
- Other hammers

6.3.1. Other geometries

For starters, other geometries can be tried out in order to find an optimized layout that provides low fatigue damage during installation, whilst maintaining a large reduction in surface area, and thus lower hydrodynamic loads. Another option can also be to thicken the structure around the perforation in order to reduce the stresses, whilst maintaining the same reduction in hydrodynamic loads. The main takeaway from this research is that ellipses in the longitudinal direction can help significantly in the reduction of stress concentrations, but there is still plenty of room to optimize the geometries analyzed in this thesis.

Furthermore, it is also important to try and avoid crossing the butt-welds with the perforations. Crossing the butt-welds will significantly increase the stress concentrations and hence the fatigue damage. Avoiding these butt-welds can cause a reduction in fatigue damage of up to a factor of 4, as shown in section 4.4.

6.3.2. Other loads and failure modes

Before the perforated monopile can be taken into use, it must also be ascertained that the structure is capable of surviving other loads as well. Hydrodynamic loads analyzed in previous research [34] [59] and installation loads analyzed here are just a part of the loads that monopiles are subject to at sea. Ice loads, wind loads, and seismic loads are other very important loads to take into account to ensure the monopile performs as expected for the entire lifetime of the monopile, without failure.

Furthermore, other failure states also need to be taken into account. This research looked into the fatigue limit state, but other limit states also need to be analyzed. The ultimate and accidental limit states can also prove to be limiting factors. Especially in geometry 4, there is a risk of buckling due to the slenderness of the structure, and the large size of the perforations.

6.3.3. Other hammers

In this research, impact hammer IHC-S-4000 was used, as well as vibro-hammer QU-CV640. First of all, a larger vibro-hammer may provide a reduced total fatigue damage, whilst still being able to install the monopile to the full intended depth of penetration. In section 5.3.2 it was mentioned that, using a vibratory hammer, the total fatigue damage was halved compared to the installation of a non-perforated monopile with the impact hammer for the same depth. For geometry 2, the fatigue damage with the vibro-hammer was only a quarter of what would be the case for the impact hammer. So far no bigger vibro-hammers are available on the market, but up to four QU-CV640 vibro-hammers can be combined to install larger monopiles. [60] If this combination of vibro-hammers can be utilized for the perforated monopile, perhaps a total reduction in fatigue damage is possible.

Interesting research is also being done about the so-called 'Gentle Driving of Piles', or GDP. This installation technique can also be used to install this perforated monopile. Using these other types of hammers can prove very interesting to achieve a reduction in fatigue damage, in combination with the other advantages that these other hammers may bring, like a reduction in installation noise.

References

[1] Wikimedia. *File:Alpha Ventus Windmills.JPG*. 2009. URL: https://commons.wikimedia.org/wiki/File:Alpha_Ventus_Windmills.JPG (visited on 01/15/2024).

[2] D.H. Meadows, D.L. Meadows, J. Randes, and W.W. Behrens. *The Limits to Growth*. Potomac Associates - Universe Books, 1972.

[3] D. Carrington and J. Mommers. *'Shell knew': oil giant's 1991 film warned of climate change danger*. 2017. URL: https://www.theguardian.com/environment/2017/feb/28/shell-knew-oil-giants-1991-film-warned-climate-change-danger (visited on 02/24/2023).

[4] Our World In Data. *Energy consumption by source*. 2022. URL: https://ourworldindata.org/grapher/energy-consumption-by-source-and-country?stackMode=absolute (visited on 02/26/2023).

[5] BBC. *The rush for nickel: 'They are destroying our future'*. 2023. URL: https://www.bbc.com/news/world-asia-66131451 (visited on 01/15/2024).

[6] npr. *How 'modern-day slavery' in the Congo powers the rechargeable battery economy*. 2023. URL: https://www.npr.org/sections/goatsandsoda/2023/02/01/1152893248/red-cobalt-congo-drc-mining-siddharth-kara (visited on 01/15/2024).

[7] Youri Öhlschläger. *Exploring the feasibility of placing a wind turbine on top of an FPSO*. Master's thesis, Offshore and Dredging engineering, TU Delft, 2022. URL: https://repository.tudelft.nl/islandora/object/uuid%3A8f3cc921-a898-4fa4-9d2b-6e694a051d95.

[8] Bob van Vliet. *Hidden curriculum*. 2023. URL: https://delta.tudelft.nl/en/article/column-hidden-curriculum (visited on 01/08/2024).

[9] TU Delta. *Live blog: the occupation at TU Delft is over*. 2023. URL: https://delta.tudelft.nl/en/article/live-blog-occupation-tu-delft-over (visited on 01/08/2024).

[10] Emiel Beinema. *This is how the second teach-in at TU Delft went*. 2023. URL: https://delta.tudelft.nl/en/article/how-second-middle-east-teach-tu-delft-went (visited on 01/08/2024).

[11] Paulo Freire. *Pedagogy of the Oppressed*. Continuum, 1968.

[12] Herbert Marcuse. *One-dimensional man: Studies in the Ideology of Advanced Industrial Society*. Beacon Press, 1964, p. 129. URL: https://www.marxists.org/ebooks/marcuse/one-dimensional-man.pdf.

[13] Wikipedia. *Offshore Wind Power*. 2021. URL: https://en.wikipedia.org/wiki/Offshore_wind_power (visited on 02/26/2023).

[14] Berlingske. *Fra energiens originaler til bølgernes gulddrenge*. 2016. URL: https://www.berlingske.dk/virksomheder/fra-energiens-originaler-til-boelgernes-gulddrenge (visited on 02/24/2023).

[15] WindEurope. *Offshore wind in Europe - key trends and statistics 2020*. 2021. URL: https://windeurope.org/intelligence-platform/product/offshore-wind-in-europe-key-trends-and-statistics-2020/ (visited on 02/24/2023).

[16] Ministerie van Economische Zaken en Klimaat. *Offshore Wind Energy Roadmap 2030*. 2020. URL: https://www.government.nl/topics/renewable-energy/documents/parliamentary-documents/2018/03/27/letter-to-parliament-offshore-wind-energy-roadmap-2030 (visited on 02/27/2023).

[17] Directorate-General for Energy. *Offshore renewable energy*. 2020. URL: https://energy.ec.europa.eu/topics/renewable-energy/offshore-renewable-energy_en (visited on 02/27/2023).

[18] Koninklijk Nederlands Meteorologisch Instituut (KNMI). *North Sea wind climatology Part 1: a review of existing wind atlases*. 2014. URL: https://www.knmiprojects.nl/projects/knw-atlas/documents/reports/2014/06/01/north-sea-wind-climatology-part-1.

[19] U.S. Department of Energy. *Offshore Wind Market Report: 2022 edition*. 2023. URL: https://www.energy.gov/eere/wind/articles/offshore-wind-market-report-2022-edition.

[20] European Marine Observation and Data Network (EMODnet). *Eurpean Atlas of the Seas*. 2021. URL: https://ec.europa.eu/maritimeaffairs/atlas/maritime_atlas/#lang=EN; (visited on 08/24/2023).

[21] Rijksoverheid. *Wat kosten windparken?* 2020. URL: https://windopzee.nl/onderwerpen/wind-zee/kosten/kosten-windparken/ (visited on 03/07/2023).

[22] European Wind Energy Agency. *The next step for offshore wind energy.* 2013. URL: https://windeurope.org/about-wind/reports/deep-water/.

[23] European wind energy association. *The European offshore wind industry-key trends and statistics 2015.* 2016. URL: https://windeurope.org/about-wind/statistics/offshore/key-trends-2015/.

[24] J.M.J. Journée and W.W. Massie. *Offshore Hydromechanics*. 1st ed. CITG Section Hydraulic Engineering, 2000.

[25] D. Kallehave, B.W. Byrne, C. LeBlanc Thilsted, and K. Kousgaard Mikkelsen. "Optimization of monopiles for offshore wind turbines." In: *The Royal Society* (2015).

[26] DNV-GL. *DNV-ST-0126 Support structures for wind turbines*. 2016. URL: https://www.dnv.com/energy/standards-guidelines/dnv-st-0126-support-structures-for-wind-turbines.html.

[27] K. Thomsen. *Offshore wind: a comprehensive guide to successful offshore wind farm installation*. Academic Press, 2014.

[28] NREL. *A Comparison Study of Offshore Wind Support Structures with Monopiles and Jackets for U.S. Waters*. 2016. URL: https://www.nrel.gov/docs/fy16osti/66099.pdf.

[29] Z. Jiang. "Installation of offshore wind turbines: A technical review". In: *Renewable and Sustainable Energy Reviews* (2021). URL: https://doi.org/10.1016/j.rser.2020.110576.

[30] M. Dolores Esteban, J.S. López-Gutiérrez, and V. Negro. "Gravity-Based Foundations in the Offshore Wind Sector". In: *Journal of Marine Science and Engineering* (2019). URL: https://doi.org/10.3390/jmse7030064.

[31] New Atlas. *HyWind - world's first floating wind turbine reaches its final destination*. 2009. URL: https://newatlas.com/hywind-floating-wind-turbine/11961/ (visited on 04/27/2023).

[32] Wikipedia. *Floating wind turbine*. 2023. URL: https://en.wikipedia.org/wiki/Floating_wind_turbine (visited on 04/27/2023).

[33] Kun Xu. "Design and Analysis of Mooring System for Semi-submersible Floating Wind Turbines in Shallow Water". In: (2015).

[34] J. Andersen, R. Abrahamsen, T. Andersen, M. Andersen, T. Baun, and J. Neubauer. "Wave load mitigation by perforations of monopiles". In: *Journal of Marine Science and Engineering* (2020). URL: https://dx.doi.org/10.3390/jmse8050352.

[35] J.F. van der Ploeg. *Perforations of Monopiles to Reduce Hydrodynamic Loads and Enable use in Deep Waters*. Master's thesis, Offshore and Dredging Engineering, TU Delft, 2021. URL: https://repository.tudelft.nl/islandora/object/uuid%3A91eada6f-4f2b-4ae6-be59-2b5ff0590c6f.

[36] E. Kementzetzidis, F. Pisanò, A.S.K. Elkadi, A. Tsouvalas, and A.V. Metrikine. "Gentle Driving of Piles (GDP) at a sandy site combining axial and torsional vibrations: Part II - cyclic/dynamic lateral loading tests". In: *Ocean Engineering* (2023). URL: https://doi.org/10.1016/j.oceaneng.2022.113452..

[37] E.A.L. Smith. "Pile-driving analysis by the wave equation". In: *American society of civil engineers* 127 (1960), pp. 1145–1193.

[38] M.F. Randolph and H.A. Simons. *An improved soil models for one-dimensional pile driving analysis*. Cambridge University Engineering Department, 1985.

[39] S.L. Lee, Y.K. Chow, G.P. Karunaratne, and K.Y. Wong. “Rational Wave Equation Model for Pile-Driving Analysis”. In: *Journal of Geotechnical Engineering* (1988). URL: https://www.researchgate.net/publication/367655480.

[40] P.C. Meijers, A. Tsouvalas, and A.V. Metrikine. “The Effect of Stress Wave Dispersion on the Drivability Analysis of Large-Diameter Monopiles”. In: *Procedia Engineering* (2017). URL: https://doi.org/10.1016/j.proeng.2017.09.272.

[41] J. Chung, R. Wallerand, and M. Helias-Brault. “Pile Fatigue Assessment During Driving”. In: *Procedia Engineering 6* (2013), pp. 451–463.

[42] I. Kourelis, S. Kontoe, R. Buckley, and A. Galbraith. “An assessment of pile driveability analyses for monopile foundations”. In: *11th International Stress Wave Conference* (2022).

[43] R.S. Stevens, E.A. Wilsie, and T.H. Turton. “Evaluating Pile Driveability for Hard Clay, Very Dense Sand, and Rock”. In: *Offshore Technology conference, Paper OTC 4205* (1982).

[44] American Petroleum Institute. *API RECOMMENDED PRACTICE 2A-WSD (RP 2A-WSD). Recommended practice for planning, designing and constructing fixed offshore platforms - Working Stress Design*. 2007. URL: https://communities.bentley.com/cfs-file/__key/communityserver-discussions-components-files/343644/API-RP-2A-WSD-2007.pdf (visited on 01/15/2024).

[45] International Standards Organisation. *Petroleum and natural gas industries — Fixed steel offshore structures*. 2007. URL: https://www.jstra.jp/html/PDF/ISO_19902_2007.pdf (visited on 01/15/2024).

[46] DNV-GL. *Fatigue Design of Offshore Steel Structures*. 2011. URL: https://cdm.ing.unimo.it/dokuwiki/_media/wikitelaio2017/rp-c203.pdf (visited on 01/15/2024).

[47] Y.K. Chow and A.M. ASCE. “Three-dimensional analysis of pile groups”. In: *Journal of Geotechnical Engineering* (1988).

[48] A.J. Deeks. *Numerical Analysis of Pile Driving Mechanics*. PhD thesis, Department of Civil Engineering, University of Western Australia, 1992. URL: http://dx.doi.org/10.13140/RG.2.1.1526.1606.

[49] G. Barauskis and F. Jakobsen. “Drivability of Large-diameter Piles With Submerged Conical Sections”. In: *Twenty-second International Offshore and Polar Engineering Conference* (2012). URL: https://onepetro.org/ISOPEIOPEC/proceedings-abstract/ISOPE12/All-ISOPE12/12249.

[50] NREL. *Definition of the IEA Wind 15-Megawatt Offshore Reference Wind Turbine*. 2020. URL: https://www.nrel.gov/docs/fy20osti/75698.pdf.

[51] D. Cathie, C. Jaeck, E. Ozsu, and S. Raymackers. “Insights into the drivability of large diameter piles”. In: *International Symposium on Frontiers in Offshore Geotechnics* (2020).

[52] IHCIQIP. *Installation of Large-Diameter Monopiles: Current practice and challenges*. 2017. URL: https://www.offshorewindenergy.org/EUROS/wp-content/uploads/2017/11/Seminar222.pdf (visited on 09/24/2023).

[53] G. Perikleous, O. Zarzouras, A. Crochelet, T. Lamant, and D. Cathie. “Energy losses during driving due to tapered section of monopile”. In: *Ocean Engineering* (2023). URL: https://doi.org/10.1016/j.oceaneng.2023.114184.

[54] A.J. Deeks and M. Randolph. “Analytical modeling of hammer impact for pile driving”. In: *International journal for numerical and analytical methods in geomechanics* (1993). URL: https://doi.org/10.1002/nag.1610170502.

[55] Ansys. *ansys mechanical user guide*. 2015. URL: https://vdocuments.net/ansys-mechanical-user-guide.html?page=1606 (visited on 01/08/2024).

[56] G. Perikleous, T. Stergiou, and S. Meissl. “An assesment of the accuracy of SRD methodologies for OWF monopile installation against a north europe driving records database”. In: *4th International Symposium on Frontiers in Offshore Geotechnics* (2023). URL: https://doi.org/10.1016/j.oceaneng.2023.114184.

[57] R. M. Buckley, M. Maron, F.C. Schroeder, and P. Barbosa. “Comon pitfalls of pile driving resistance analysis - A case stufy of the wikinger offshore wind farm”. In: *8th international conference on offshore site investigations and geotechnics: Smarter solutions for future offshore developments. Volume 2.* (2017).

[58] V. Nguyen, C.R. Parthasarathy, and V. Goel. “Fatigue damage after installation of an offshore-friven pile-back analysis from pile monitoring data”. In: *Advances in Offshore Geotechnics, pp 303-318* (2020). URL: https://doi.org/10.1007/978-981-15-6832-9_17.

[59] G.A.S. Gonzalez. *Advantages and Challenges of Perforated Monopiles in Deep Water Sites*. Master’s thesis, Offshore and Dredging engineering, TU Delft, 2023. URL: https://repository.tudelft.nl/islandora/object/uuid%3A490791b6-a912-4bac-a007-f77012c01107.

[60] CAPE Holland. *Offshore vibro technology*. 2022. URL: https://capeholland.com/wp-content/uploads/2022/02/Version-03-2022_CAPE-Holland_Offshore-Vibro-Technology_.pdf (visited on 01/08/2024).

A

Additional figures and code

Source code for figure 3.3 based on Deeks and Randolph [54]

```
clear all
clc

r1 = 5;                                 % ouside radius monopile
r2 = 5-0.062;                           % inside radius monopile
A = pi * (r1.^2 - r2.^2);               % area
E = 210*10^9;                           % Young's modulus steel
c_p = 5000 ;                            % m/s speed of sound in steel
k_c = 3.5*10^9;                         % cushion stiffness N/m
m_r = 1976.36;                          % Ram weight kN
m_a = 489;                              % anvil weight kN
Z =  2.3e+06 ;                          % Impedance in Ns/m, by E*A/c_p
A2 = 11.8907;                           % Ram area2 in m^2 from GRLWEAP

m_a_star = m_a./m_r;                    % dimensionless anvil mass
k_c_star = k_c * m_r ./(Z.^2);          % dimensionless cushion stiffness
mu = sqrt((k_c_star.^2)./4 - k_c_star);
mu_accent = sqrt(k_c_star-(k_c_star.^2/4));


a0 = k_c_star./m_a_star;
a1 = k_c_star*(1./m_a_star + 1);
a2 = 1./(m_a_star);

alfa = a1*a2./6 - a0./2 - (a2.^3)./27;
beta = sqrt((a1.^3)./27 - (a1.^2 * a2.^2)./108 -(a0*a1*a2)./6 + (a0.^2)./4 + (a0*a2.^3)./27);

b1 = a2./3 - (alfa + beta).^(1./3) - (alfa - beta).^(1./3);
b2 = a2./3 + 0.5*((alfa + beta).^(1./3) + (alfa - beta).^(1./3));
omega = sqrt(3)./2 * ((alfa + beta).^(1./3) - (alfa - beta).^(1./3));

c1 = b1;
c2 = b2 - b1;
phi = atan(c2./omega);
F_p = a0./(omega.^2+c2.^2);

rangeArray = 0:0.0001:0.01;

t_star = Z/m_r.*rangeArray;
f_p_star3 = t_star.*exp(-k_c_star./2 .*t_star);

hold on
plot((1000.*rangeArray),E*A2./c_p.*f_p_star3./1000) %factor 1000 to accomodate for
    milliseconds and kN, E*A2./c_p to reverse non-dimensionality
xlabel({'time in ms'});
ylabel({'Force in kN'});
```

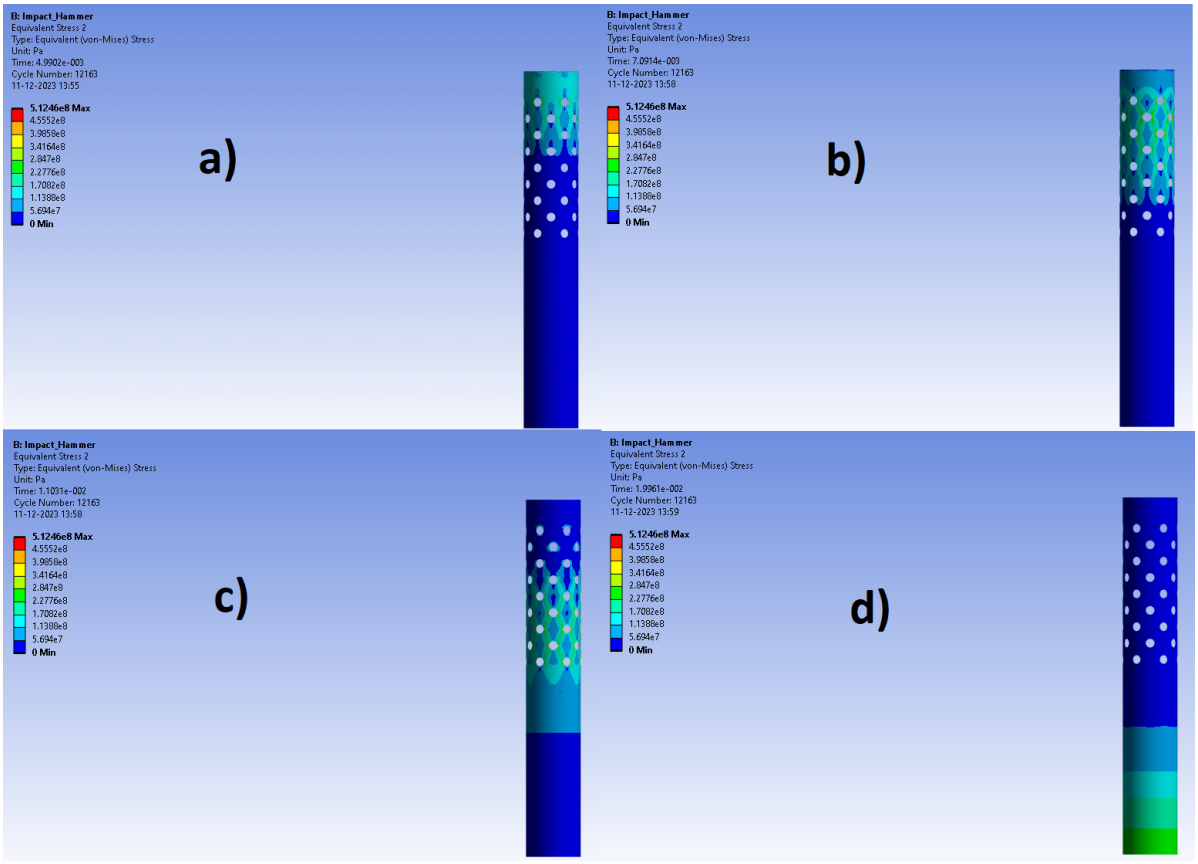

Figure A.1: Force wave propagation through perforated monopile with geometry 1 using an element size of 0.2 meters. The stresses are displaced at 5, 7, 11 and 20 milli-seconds

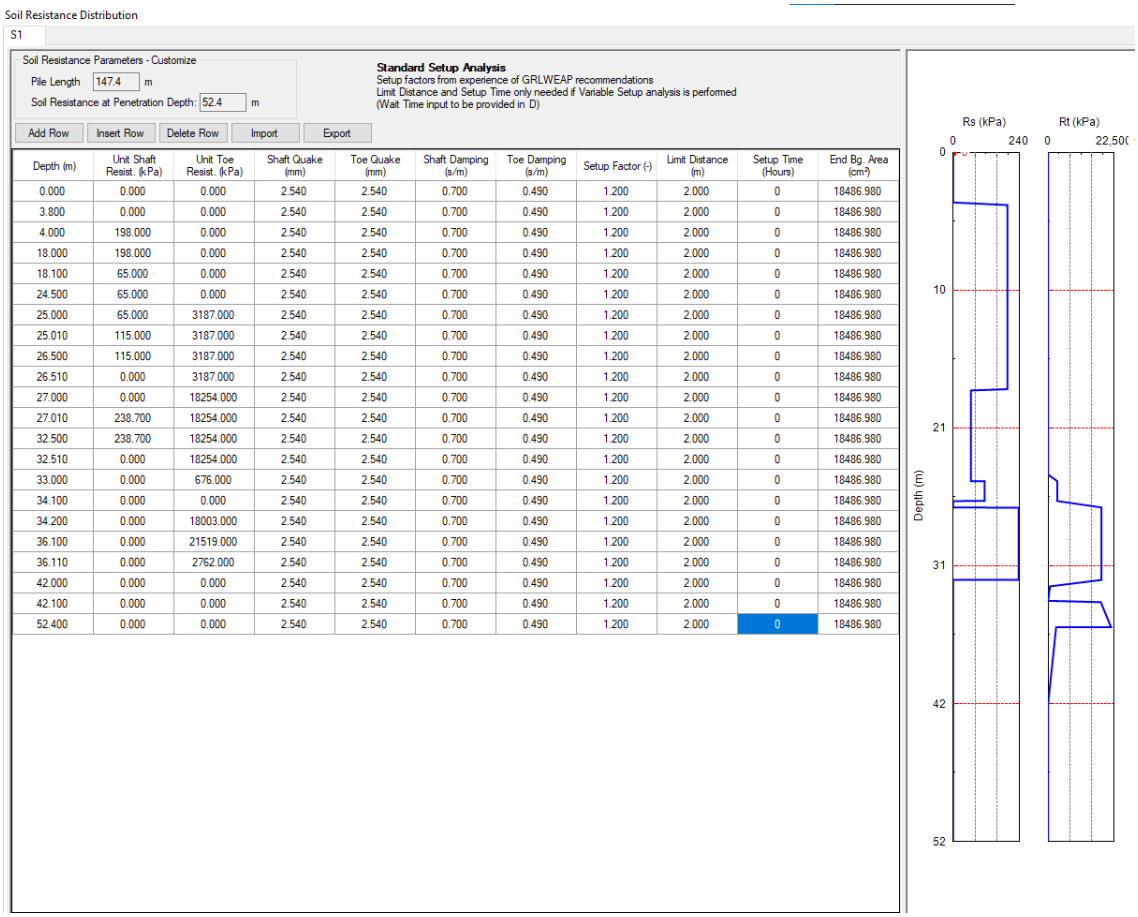

Figure A.2: All the soil parameters used as an input for the GRLWEAP software, which is used as a resistance for the wave equation

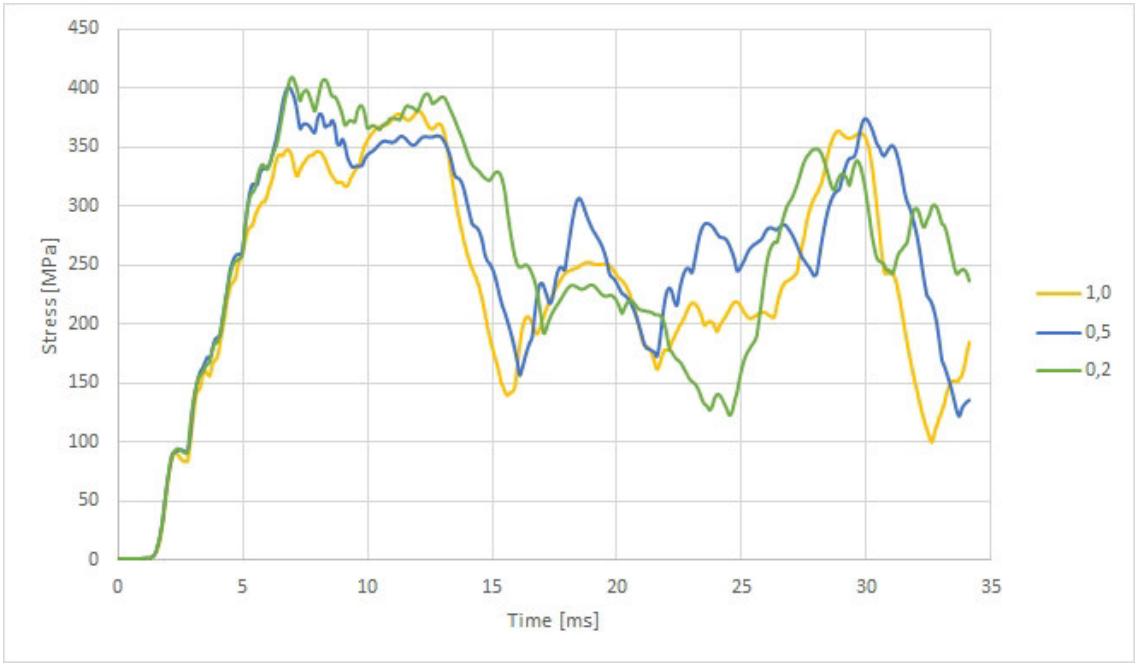

Figure A.3: Mesh convergence for the stresses in the perforated monopile with geometry 2 with the element size in meters

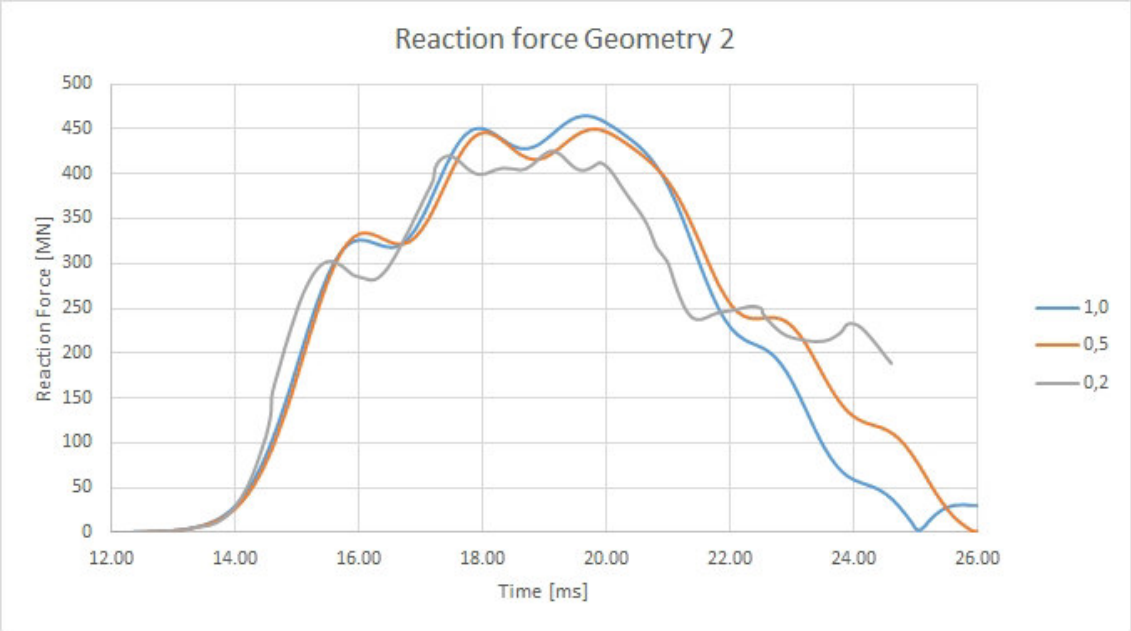

Figure A.4: Mesh convergence for the reaction force in the perforated monopile with geometry 2 with the element size in meters

B

Additional figures for reduced force input

Additional figures for the results described in section 5.3.3, showing stresses, reaction forces and velocities.

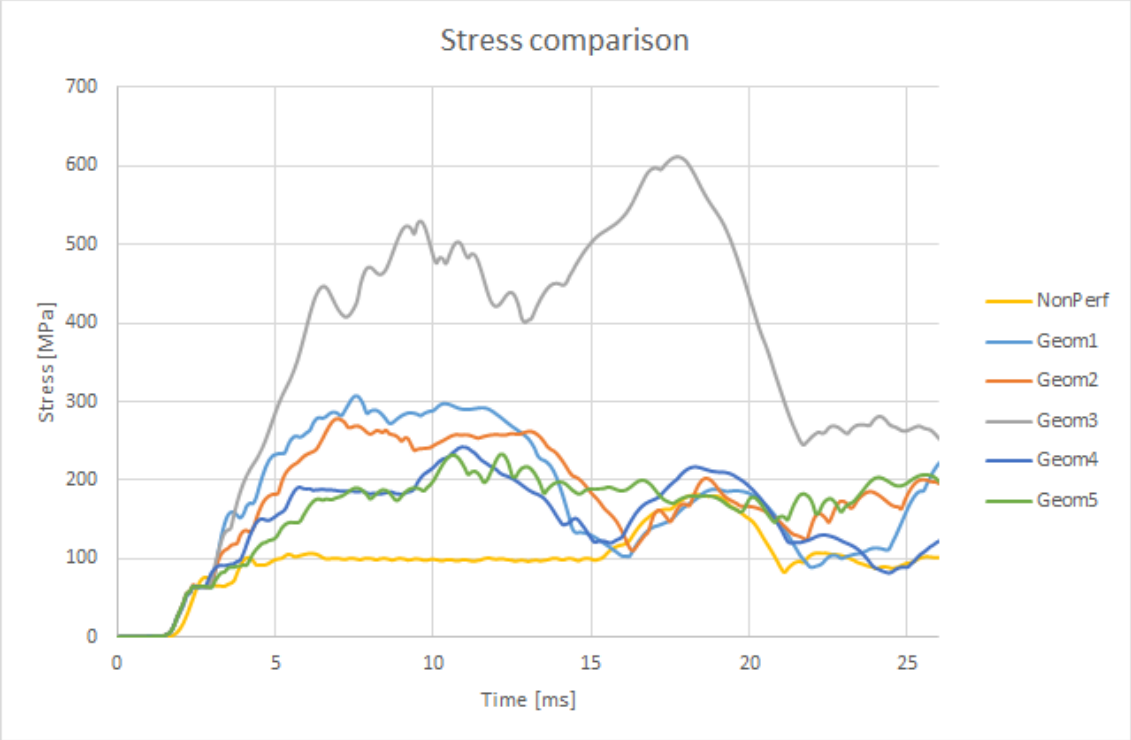

Figure B.1: The maximum stress concentration observed in all geometries of the perforated monopiles over time, using half the installation force available in IHC-S-4000

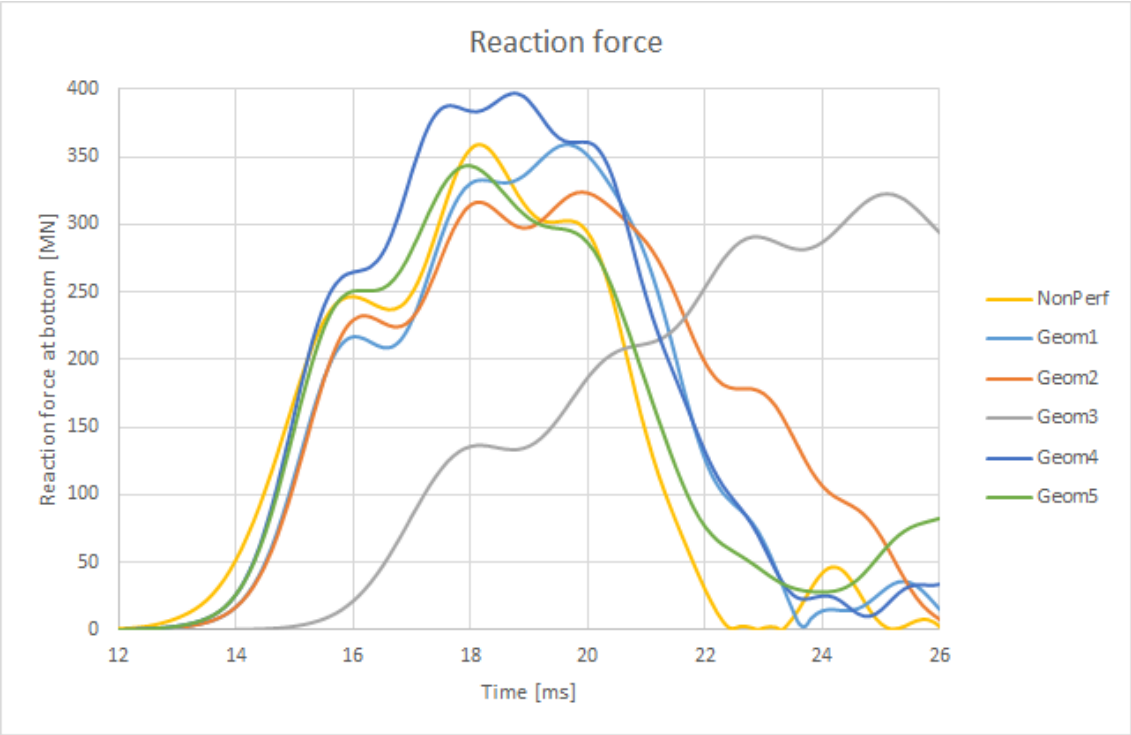

Figure B.2: The reaction force at the bottom of the model for all geometries over time, using half the installation force available in IHC-S-4000

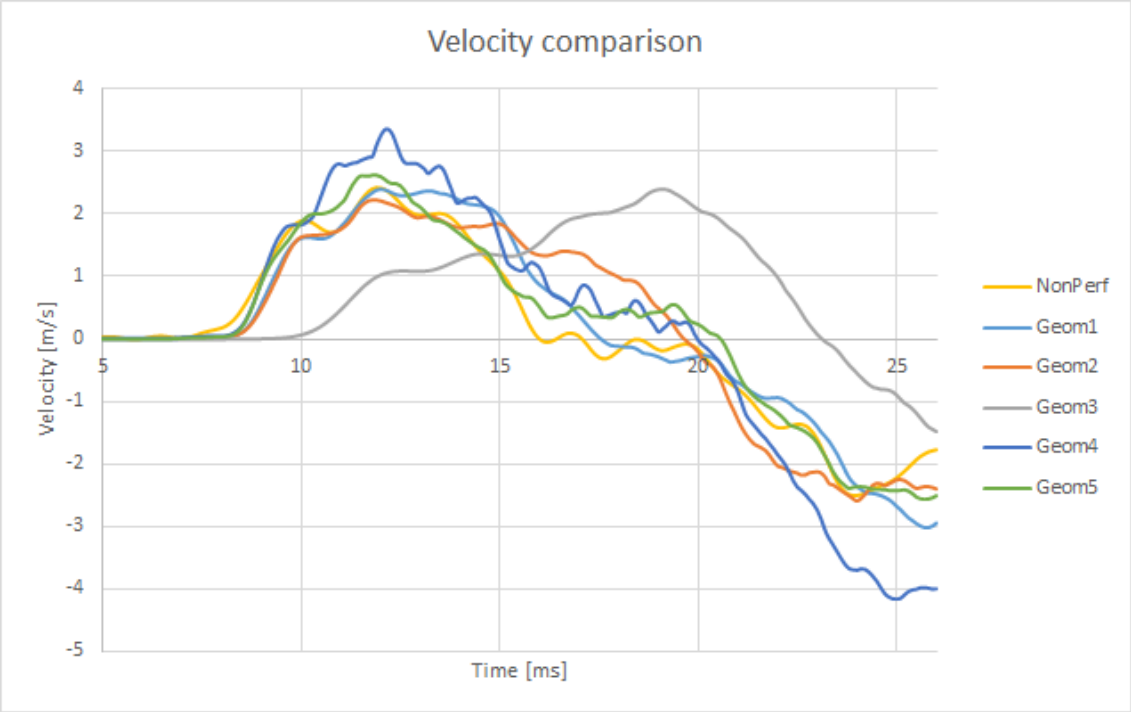

Figure B.3: The velocity of the probe located 30m from the bottom of the model in all geometries of the perforated monopiles over time, using half the installation force available in IHC-S-4000